REPORT

IEA Wind TCP Task 32: Comparative Exercise on Ground Based Lidar in Complex Terrain

Authors: Alexander Stökl (Energiewerkstatt e.V.)

Sara Koller (Meteotest AG)

Johannes Cordes (Deutsche WindGuard Consulting GmbH)

Oliver Grüning (Ramboll Deutschland GmbH)

Andrew Black (Vaisala France)

Atsushi Yoshimura (Green Power Investment)

Revision 0 – December 2022
Revision 1 – May 2023: style of subsection heading, added missing references to Sect. 7

Executive summary

The present report summarizes the results of a comparative exercise aimed to investigate the application of vertical profiling wind LiDAR (Light Detection And Ranging) in complex terrain and of correction methods to reduce the errors and uncertainties of LiDAR in complex terrain. The comparative exercise has been conducted from 2019 to 2022 in the framework of IEA Wind Task 32/52 “Wind LiDAR”. This report has been prepared by the authors listed on the title page who take the responsibility for the results and the opinions given in the report.

Several sets of LiDAR measurements from complex terrain sites have been made available for this study. At all sites, reference data from co-located and parallel met mast measurements are available. Comparison of the LiDAR measurements with co-located reference met masts confirmed, that the LiDAR measurements are significantly affected by the complex terrain flow conditions. Overall, eleven different sets of corrections to the LiDAR data, different numerical methods and different parametrizations, have been computed for the considered sites.

Due to the small and restricted ensemble of datasets in this study (five sites from the Austrian Alps), it was not possible to draw any robust conclusions on the applicability of LiDAR and LiDAR correction methods in complex terrain. Nevertheless, this exercise exemplifies the significant challenges of LiDAR measurements in complex terrain and illustrates the many effects and uncertainties that need to be considered. The present report thus focuses on the presentation of the results of the comparison between LiDAR and met mast, the applicability of the correction methods, and on possible ways to characterize terrain complexity and flow complexity.

Table of Contents

Executive summary ii
1. Introduction 1
  1.1. Description of the Problem 1
  1.2. Volume versus point measurement 3
  1.3. LiDAR correction versus site calibration 3
2. Datasets 4
  2.1. Technical description of the measurements 10
  2.2. Data processing 11
3. Correction methods 12
4. Results 18
  4.1. Comparison of LiDAR and Met mast data 18
  4.2. Flow characteristics in LiDAR data 24
  4.3. Terrain characterization 27
  4.4. Corrected LiDAR data 31
5. Understanding LiDAR/Mast Deviations 36
  5.1. Correlation with terrain complexity metrics 36
  5.2. Correlation with wind field structure 38
  5.3. Numerical site calibration 38
6. Summary & conclusions, need for further activities 40
7. List of References 41

1. Introduction

For the current generation of large onshore wind turbines, with hub heights in excess of 150 m, wind LiDAR (Light Detecting And Ranging) has become an essential tool for providing accurate estimates of annual energy yields and site wind conditions for load analysis. Ground based, vertical profiling wind LiDAR can easily measure at the required heights and has significant advantages over met masts in regard to costs and ease of installation. Vertical profiling wind LiDARs are therefore used in many onshore wind energy projects. In addition, LiDAR devices have almost completely replaced meteorological masts for offshore applications in Europe.

At the same time, complex terrain and complex flow remain a persistent obstacle for stand-alone wind LiDAR measurements (Clifton, et al., 2015). Beside the systematic difference between a cup anemometer (point) measurement and a LiDAR (volume) measurement, a wind LiDAR measurement in complex terrain can be significantly affected from flow inhomogeneity, introducing an additional measurement uncertainty of unknown magnitude. To some degree, it is possible to correct these complex terrain errors with numerical flow models. Despite recent favorable reports (Black, et al., 2020) on correction methods for wind LiDAR in complex terrain, the overall applicability of such methods, and of vertical profiling wind LiDAR in complex terrain in general, remains unclear. One of the key challenges in assessing the usability of wind LiDAR in complex terrain is the large diversity in site conditions, including terrain orography, surface roughness, vegetation, and flow stratification, making it hard to transfer experience from one site to the other.

As a contribution to this discussion, we present in this report results from parallel met mast and LiDAR measurements from five Austrian wind energy sites in complex terrain together with several sets of correction factors to these LiDAR measurements and an assessment of the terrain complexity at the investigated sites.

The challenges of complex terrain and complex flow are not exclusive to LiDAR measurements but would affect remote sensing devices (RSD) in general. The analysis and the assessment methods described herein would therefore also apply in a very similar way to SoDAR (Sound Detecting And Ranging) measurements in complex terrain. However, since the present report specifically deals with LiDAR measurements, the term LiDAR has been used in preference to the more general term RSD.

1.1. Description of the Problem

In complex terrain, especially in the lower layers of the boundary layer, the wind flow is affected by the topography and follows the terrain contours. Therefore, the wind vector is not necessarily horizontal and homogeneous, as it would be in flat terrain, but there is also a vertical component that needs to be considered when describing the wind vector. A wind LiDAR device measures the wind speed along the line of sight. Different scanning patterns can be used to measure wind speeds in vertical profiling LiDARs (Clifton, et al., 2015). A typical setup involves four beams that are tilted by about 30° from the vertical in the four cardinal directions. Optionally, a fifth beam is used in the vertical axis to directly access the vertical component of the wind speed. This is also the case for the Windcube v2 units, that have been used to record the datasets used in this study. The line-of-sight Doppler wind speeds measured along the beams are then combined, as illustrated in Figure 1, to arrive at a result for the wind speed vector (horizontal and vertical components) at a height above the LiDAR device.

This wind speed reconstruction combines information that is recorded in different volumes, and, according to the scanning pattern used, recorded at somewhat different points in time. According to the tilt of the beams of about 30° from the vertical, the horizontal distance between the measurement volumes at the beams is about the same as the corresponding measurement height. The geometric wind speed reconstruction thus relies on the presumption, that the wind field is homogeneous in the measurement domain within the inverted pyramid formed by the four corner beams and that the wind field is constant for the duration of a scanning pattern.

Depending on the power and the measurement principle of the LiDAR device, wind speeds can be measured simultaneously in several heights up to a total height of several 100 m. Accordingly, the measurement volumes are then separated by about the same distance horizontally. In complex terrain, significant flow inhomogeneities may be present at such length scales, in addition to temporal variability and unsteady flows. A wind LiDAR measurement in complex terrain can thus be significantly affected by the flow conditions in complex terrain, resulting in larger measurement errors and a higher measurement uncertainty.

By numerical modelling or measuring of the flow conditions in the measurement domain, the effects of the flow conditions on the particular LiDAR measurement geometry can be anticipated. Expressed as correction factors, these can then potentially be used to reduce the measurement errors of the LiDAR and to improve its accuracy.

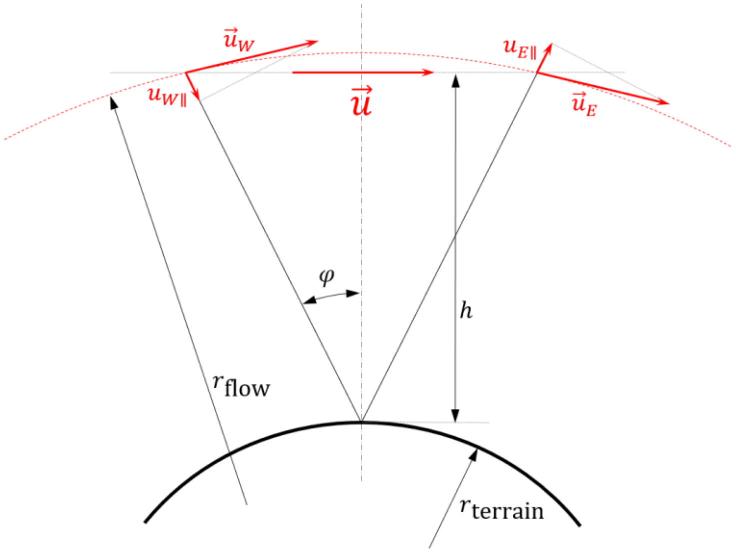

Figure 1: Two-dimensional scheme of ground-based LiDAR measurement.

From the geometry illustrated in Figure 1, the horizontal wind speed (in East-West direction) measured by the LiDAR $u_{x\text{ LiDAR}}$ can be reconstructed as:

$$u_{x\text{ LiDAR}} = \frac{u_{E\parallel} - u_{W\parallel}}{2\sin\varphi}$$

The symbols in Figure 1 are:

h	Measurement height.
φ	Beam angle from vertical.
$\vec{u} = \begin{pmatrix} u_x \\ u_y \\ u_z \end{pmatrix}$	Wind speed vector at measurement position with its components in the directions East-West (x), North-South (y), and the vertical direction (z).
$\vec{u}_W$	Wind speed vector at measurement volume of left (Western) beam.

$\vec{u}_E$	Wind speed vector at measurement volume of right (Eastern) beam.
$u_{W\|}$	In-beam (parallel) component of wind speed at measurement volume of left (Western) beam.
$u_{E\|}$	In-beam (parallel) component of wind speed at measurement volume of right (Eastern) beam.
r_{flow}	Curvature radius of flow at measurement position.
r_{terrain}	Curvature radius of terrain at measurement position.

1.2. Volume versus point measurement

In addition to the measurement errors caused by the flow conditions in complex terrain, a comparison with a met mast reference measurement, taken either with a cup or an ultrasonic anemometer, also has to consider the different measurement volumes. Cup and ultrasonic anemometer are essentially point measurements, probing a volume of some 10 cm at most. In comparison, a wind LiDAR probes several volumes, where each volume, depending on measurement height, can be several meters long and wide. Furthermore, as described above, wind speed reconstruction then combines measurements from several beams that are separated by a horizontal distance on the order of the measurement height. Small scale inhomogeneities (“turbulence”) in the wind field are thus registered very differently by wind LiDAR and by met mast anemometry.

In principle, the larger measurement volume of wind LiDAR compares favorably to wind turbines, which can be seen to possess a probing volume with the size of the rotor disc. On the other hand, assessment of wind turbine site suitability, e.g. with regard to the allowed turbulence intensity, usually refers to classic (point measurement) anemometers. There is thus a continuing need to relate wind LiDAR measurements to point references.

1.3. LiDAR correction versus site calibration

When time series from wind LiDAR measurements are compared to simultaneous met mast data, this not only involves different measurement principles and different measurement volumes, but also different measurement positions. As the beams, or the cone, of the LiDAR have to clear the met mast structure and stays, a horizontal separation of some 10 m is usually needed between the met mast and the LiDAR device. In flat terrain, the difference in wind conditions for this separation would be perfectly negligible, in a complex, inhomogeneous flow, this separation of LiDAR and met mast can be very significant when comparing simultaneous wind measurement data.

For Site C, which according to our results seems to be strongly affected by complex terrain conditions, a numerical site calibration has been performed to estimate the effect of the offset between the different measurement positions. The results of this numerical site calibration are described in Section 5.3.

2. Datasets

The five sites investigated in this study are all situated in the federal state Styria in Austria. The landscape in the mountainous areas of Styria is for the most part characterized by coniferous forests and so is also the vegetation at the five investigated sites. The forested areas are structured by clearings and patches of meadows or other low vegetation. Overall, concerning its land use characterization, all areas thus exhibit quite rough surfaces leading to high turbulence intensities. Some LiDAR-devices have been set up within forest glades which measure up to 1000 m in its widest dimensions but more usual they are quite small with typical length scales of 10 m to 200 m.

Concerning the orographic situation, the sites are located in a low mountain range in transition to alpine areas. The orography on the considered sites is illustrated in Figure 2 to Figure 6. For confidentiality reasons, the figures do not give the absolute elevation but only relative heights, but nevertheless convey an impression of the mountainous orography at the sites. The main panel of each figure shows an area of about 10 km by 10 km. The inset detail view shows the close vicinity of the measurement positions including the LiDAR-position (orange symbol), approximate locations of the measurement volumes (red symbols), and the location of the co-located met-mast (“MM”, green symbol). The depiction of the measurement volumes is based on the reference height (i.e. top height of the met-mast, see Table 1) and serves to illustrate the beam orientation of the LiDAR devices.

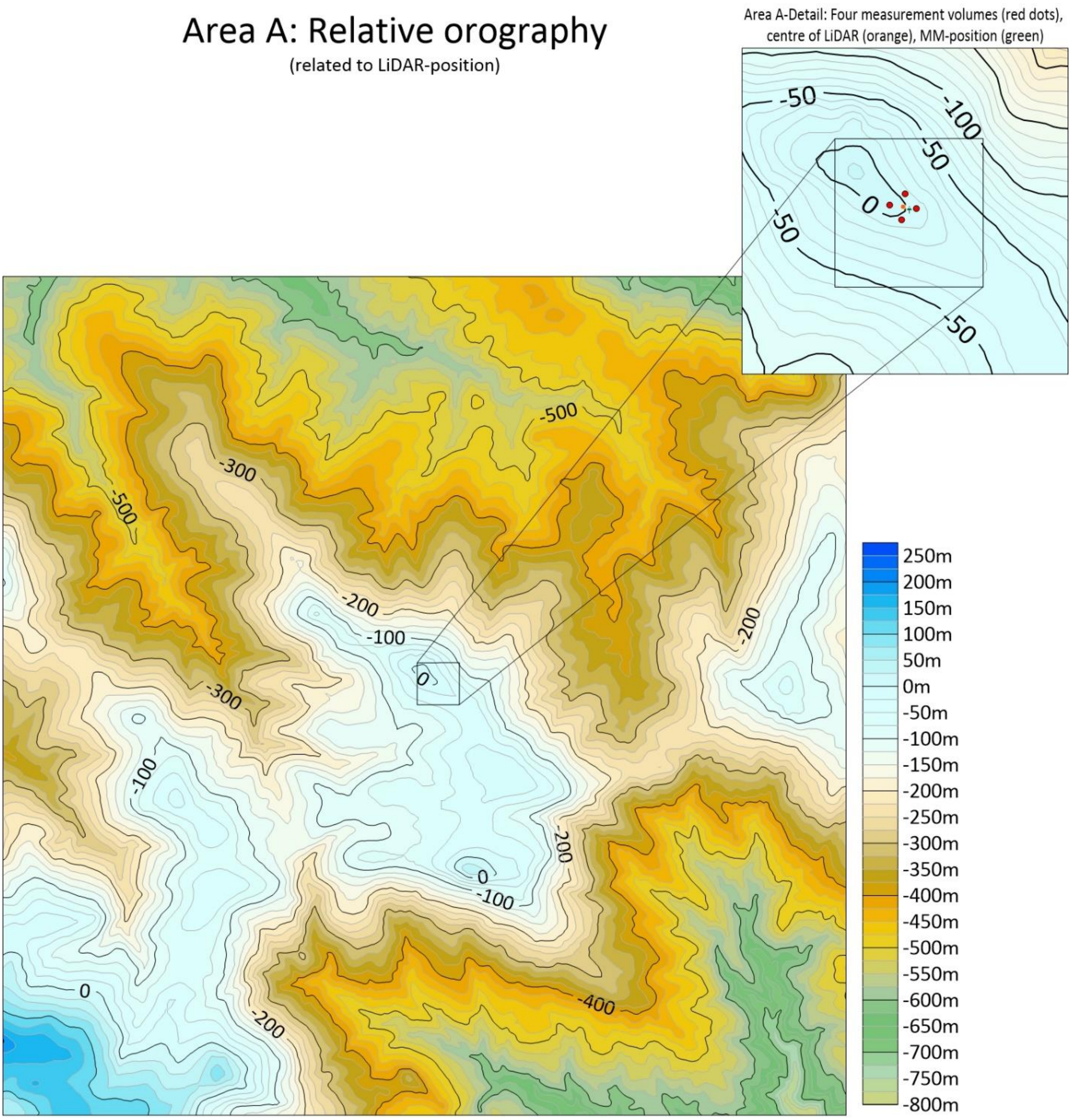

Figure 2: Relative heights (related to LiDAR-device) above see level of Area A.

At Site A, Figure 2, the LiDAR-device has been placed nearly on top of a local hill, although the highest elevations in the illustrated area can be found at some distance to the southwest (lower left corner) and lie at about 250 m above the LiDAR altitude. In the other directions, the terrain descends to lower elevations and is thus no obstacle to the wind-inflow. The relative elevation in the illustrated area ranges between about -800 m and +275 m.

At Site A, the LiDAR and the met mast have been placed in a small clearing, approx. 70 m wide. The surrounding area (~1 km radius) is predominantly forested, except for some smaller clearings and patches of reforestation. The separation between met mast and LiDAR is approximately 30 m.

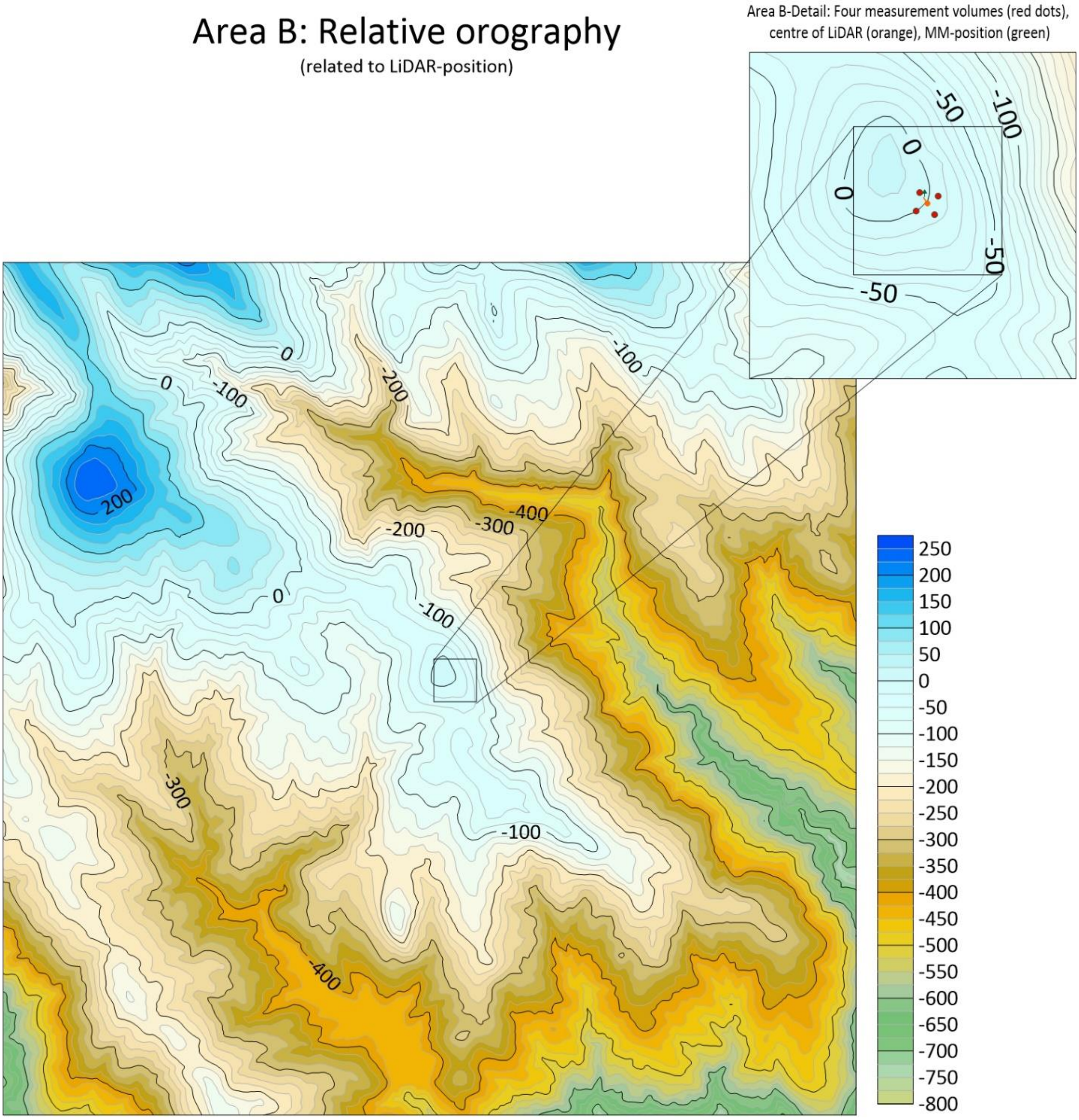

Figure 3: Relative heights (related to LiDAR-device) above see level of Area B.

The LiDAR-device on Site B (Figure 3) has also been placed nearly on the top of a hill, but a higher summit can be found in northwestern direction with an elevation of about 250 m above the LiDAR's position. To the east and south, the terrain drops to relative elevations of about -800 m.

The immediate vicinity of the LiDAR and the met mast are characterized by low vegetation (grass). The wider surrounding (1 km radius) is covered by patches of grassland and forests with different growth height. The separation between met mast and LiDAR is approximately 25 m.

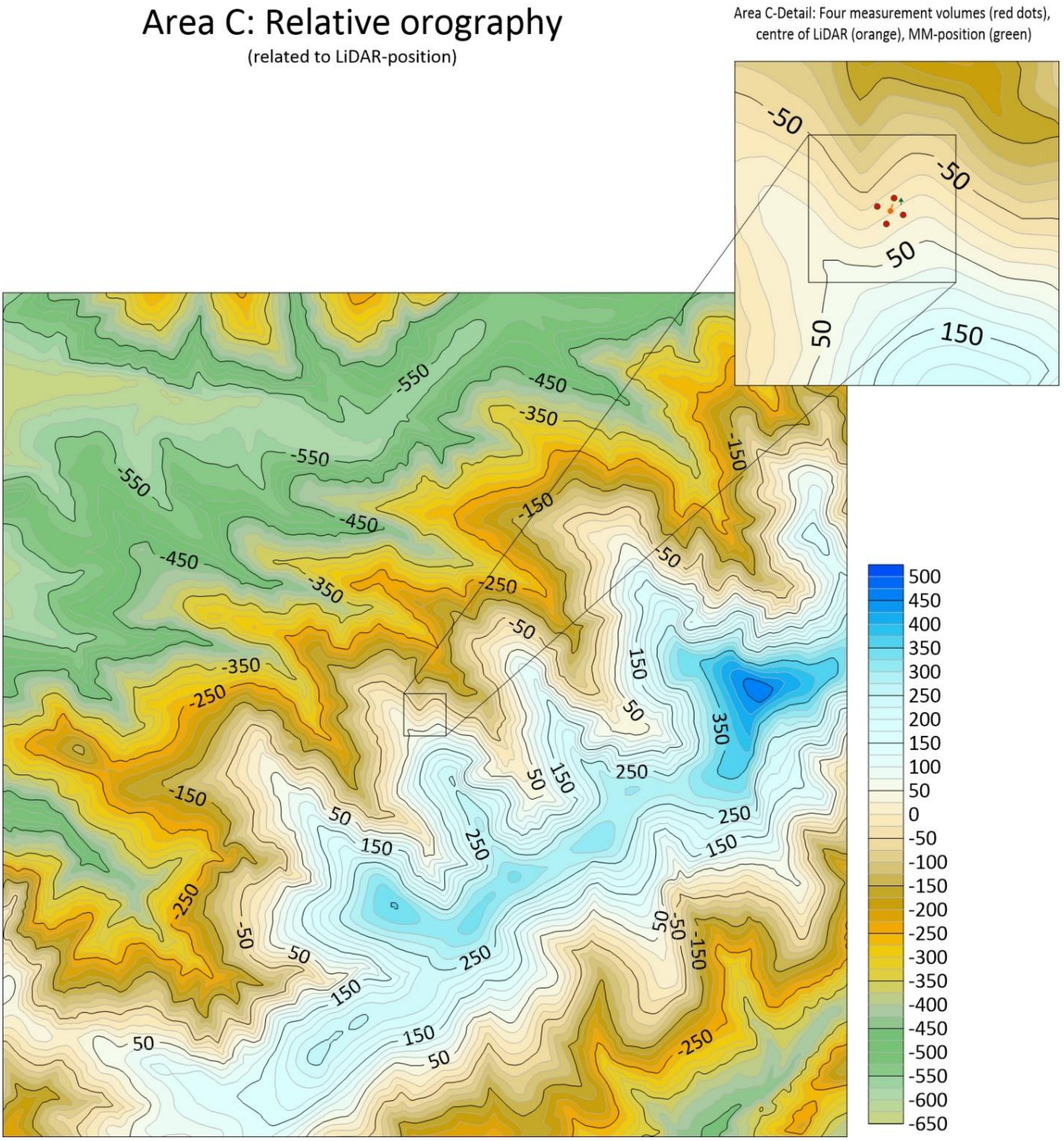

Figure 4: Relative heights (related to LiDAR-device) above see level of Area C.

At Site C, Figure 4, the LiDAR-device has been placed on a slope of a mountain chain approximately 300 m below the ridge. The ridge spreads from southwest to northeast and rises at its highest peak to about 500 m above the LiDAR’s elevation. The relative elevation in Figure 4 approximately ranges between -650 m and +525 m.

The vegetation at the measurement site is characterized by forests with varying height and growth density. In the wider surrounding, beyond 200 m, the forest is interspersed with patches of grassland. The separation between met mast and LiDAR is approximately 40 m.

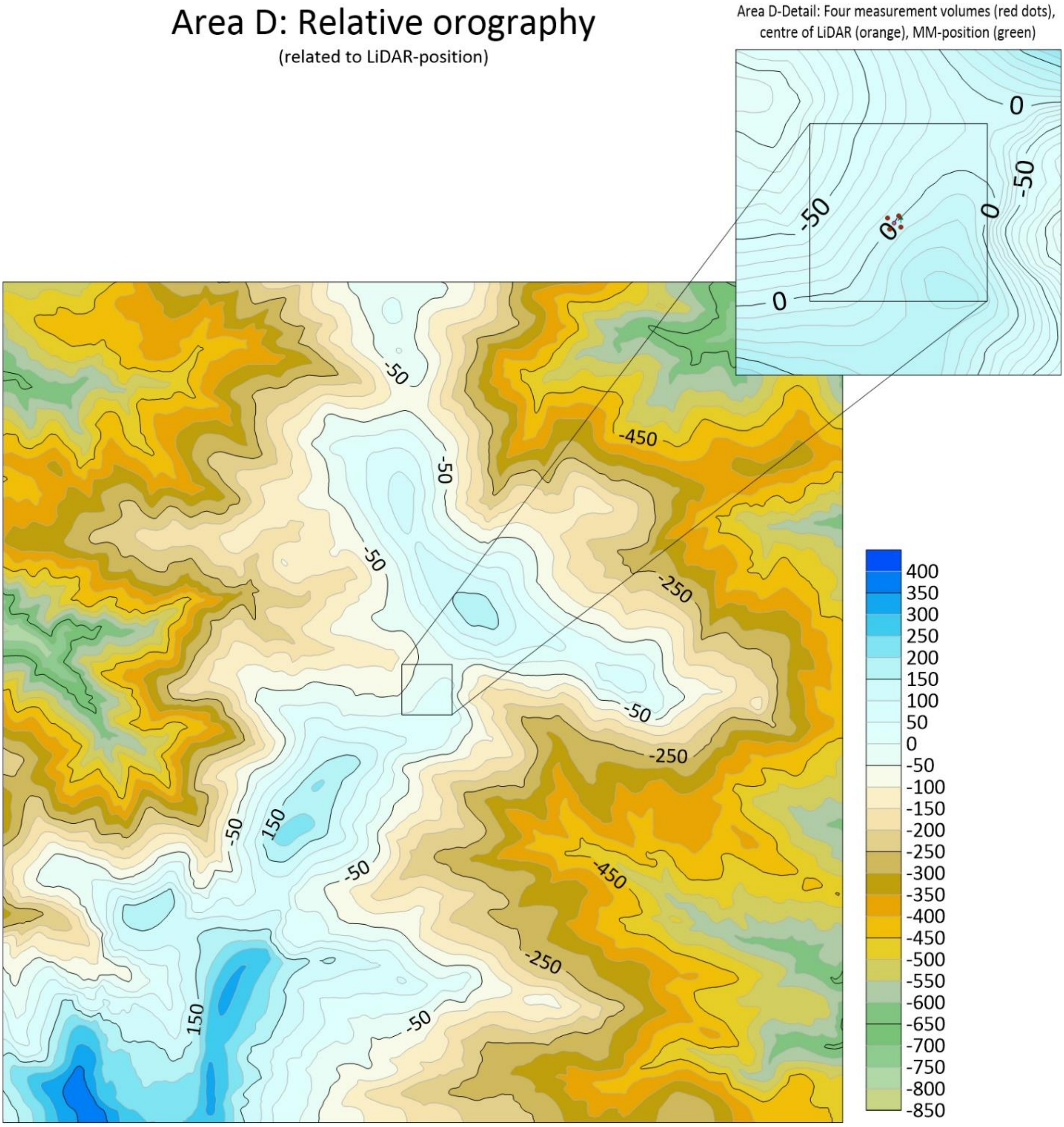

Figure 5: Relative heights (related to LiDAR-device) above see level of Area D.

The LiDAR-device in Site D (Figure 5) has been placed at a wide saddle between two close-by peaks. From this saddle, a ridge spreads to the north and in direction north-southwest. The extreme elevation in southern direction is about 400 m higher than the saddle. Overall, the relative elevation in (Figure 5) varies between approximately -850 m and +425 m.

The ridge where the measurement has been placed is dominated by grassland. On the slopes to the ridge grow individual trees that change into a sparse forest at lower elevations. The separation between met mast and LiDAR is approximately 25 m.

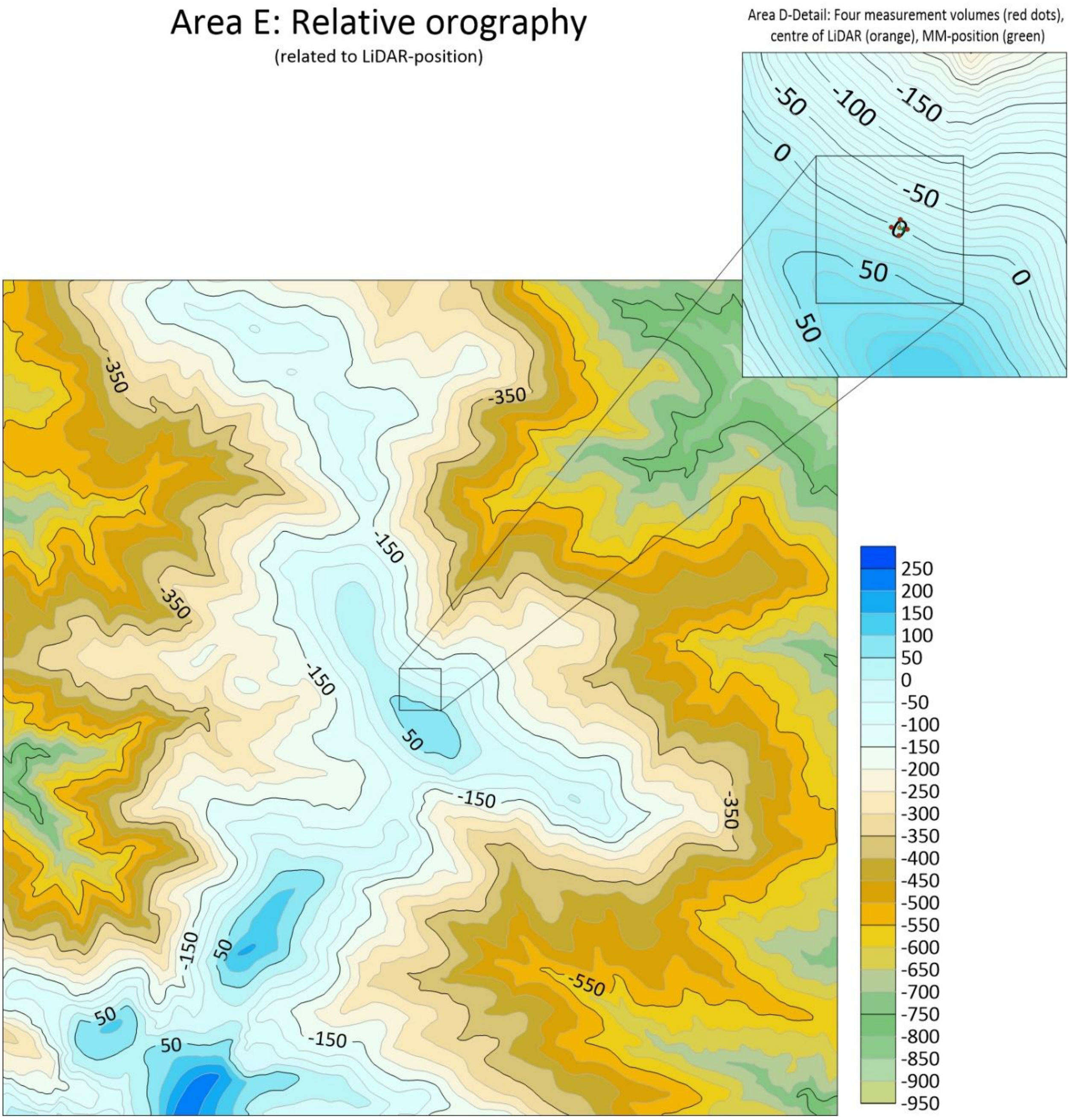

Figure 6: Relative heights (related to LiDAR-device) above see level of Area E.

At Site E, the LiDAR-device (Figure 6) has been placed somewhat offset and below (~75m) a local peak. From that peak a ridge spreads to the north and in direction south-southwest, rising in southern direction up to an elevation of about 250 m above the LiDAR position. The relative elevation in Figure 6 ranges between about -950 m and +250 m.

The met mast and the LiDAR at Site E are situated on a ridge dominated by grassland. Only at lower elevations, at distances beyond 250 m from the measurements, the grassland gradually changes into a sparse forest. The separation between met mast and LiDAR is approximately 25 m.

2.1. Technical description of the measurements

All wind LiDAR measurement where taken with ground based, pulsed LiDAR devices. Table 1 summarizes some important characteristics of the LiDAR and met-mast measurements. Calibrated anemometers and verified LiDARs have been used throughout. All measurements conform to IEC 61400-12-1 (International Electrotechnical Commission, 2017) and FGW TR6 (Fördergesellschaft Windenergie und andere Dezentrale Energien (FGW), 2021). A significant contribution to the measurement uncertainties due to off-axis response of the cup anemometers has been excluded based on an analysis comparing the cup measurements with co-located 3D ultrasonic anemometers.

	Site A	Site B	Site C	Site D	Site E
Top anemometer type	Thies, first class	Thies, first class	Thies, first class	Thies, first class	Thies, first class
Mast height	85.5 m	85.5 m	85.5 m	52.5 m	52.5 m
Vane type, height, boom orientation	Thies, first class, 83 m, 24°	Thies, first class, 83 m, 193°	Thies, first class, 83 m, 96°	Thies, first class, 48 m, 82°	Thies, first class, 48 m, 27°
Additional anemometers, height, boom orientation	Thies 3D Ultrasonic 83 m, 208°	Thies 3D Ultrasonic 83 m, 15°	Thies 3D Ultrasonic 83 m, 274°	Thies first class, 48 m, 261°	Thies first class, 48 m, 209°
Time with parallel data	6 weeks	9 weeks	5 weeks	6 weeks	6 weeks
LiDAR device	WindCube v2	WindCube v2	WindCube v2	WindCube v2	WindCube v2
Wind field reconstruction	Scalar	Scalar	Scalar	Scalar	Scalar
Setup northing	95°	222°	14°	29°	4°
Distance and difference in terrain elevation between LiDAR and met mast	Dist.: 30.5 m Elev.: 2.3 m	Dist.: 23.2 m Elev.: -2 m	Dist.: 42.4 m Elev.:0.7 m	Dist.: 24.2 m Elev.: 0.1 m	Dist.: 23.2 m Elev.: -0.2 m

Table 1: Technical characteristics of the wind measurements on the five sites.

2.2. Data processing

For the comparison between LiDAR and met mast measurements, only those time periods have been taken into account, where parallel data from both the LiDAR and met mast is available. To compute the LiDAR wind speed at the exact height of the met mast anemometer, linear interpolation between the two range gates immediately above and below has been used. Interpolation has been performed for 10-min average data.

Data samples affected by anemometer icing or by wakes from the met mast or lightning rod have been removed from met mast anemometry. For the LiDAR data, an availability threshold of 80% (per 10-min frame) has been used. For lower wind speeds, the relative amplitude of measurement uncertainties and random wind variability becomes disproportionally large. As low wind speeds are not relevant from a resource point of view, a lower wind speed cut-off of 2.5 m/s has been used for LiDAR/mast comparisons and other evaluations.

3. Correction methods

For the reconstruction of the wind speed vector from the along-beam Doppler-shift measurements, wind LiDAR devices usually rely on the assumption of a homogeneous flow. In non-uniform flow, like that experienced in complex terrain, this assumption can break down and lead to terrain-dependent measurement errors. In order to identify such situations and quantify the associated measurement uncertainties due to inhomogeneous flow conditions, different approaches and techniques are available. According to the IEC 61400-12-1:2017 (International Electrotechnical Commission, 2017), a LiDAR should be subject to a thorough analysis of the influence of non-uniform flow on measurement bias with reference to their particular configuration. According to IEC 61400-12-1:2017, the use of suitable flow models in combination with the device-specific reconstruction algorithms might be used to assess the uncertainty due to non-homogeneous flow and to correct the biased measurement data accordingly. A simplified method to estimate the terrain dependent measurement error is given by the geometrical approach used by (Bingöl, Mann, & Foussekis, 2008), with extensions by (Albers, Janssen, & Mander, 2010).

In the present comparative exercise, several different approaches and techniques have been applied and compared. The subsections and tables below describe the modelling assumptions and methods used by the participants for the considered sites. These include different types of flow-models that may include the effect of forested areas, thermal stability, and site-specific surface roughness. Based on the device-specific reconstruction algorithms, the reconstructed horizontal wind speed (reconstructed from the radial wind speeds along the beams) yields a correction factor when compared with the horizontal wind speed in the flow model at the LiDAR’s measurement position.

Method GPI (Green Power Investment)

The flow correction factor, relating between the horizontal wind speed measured by the wind LiDAR and the horizontal wind speed recorded by the met mast to anemometer, is calculated using a Large Eddy Simulation (LES).

This involves four steps: (1) The velocity vector is extracted from the simulation at the locations where the LiDAR is probing the flow field. (2) At each measuring location, the line-of-sight velocity along the beam is evaluated by projecting the velocity vector onto the beam axis. (3) The reconstruction algorithm used by the LiDAR device is then used to calculate horizontal wind speed as it would be recorded by the LiDAR. (4) The flow correction factor is calculated as the ratio between the horizontal wind speed from the numerical model at the LiDAR’s location and in the relevant height, and the calculated horizontal wind speed as it would be measured by the LiDAR. The flow correction factor has been evaluated in 16 sectors of wind direction.

For the numerical modelling, the CFD model RIAM-COMPACT (Uchida & Takakuwa, 2020) (Uchida & Ohya, 2011) has been used, which was developed at Kyushu University. Table 2 summarizes the parameter used for the modelling by GPI.

	Units	Site A	Site B	Site C	Site D	Site E
Modelling specs						
Modelling approach	-	LES				
Flow model	-	Riam Compact				
Correction approach	-	Standard correction of flow curvature only				
Forest modelling approach	-	-				
Stability considered	-	Version 1: not included Version 2: combined stable and neutral				
Input data						
Roughness input data	-	Forest, same value				
Elevation data	-	SRTM – 1 arc second				
Mesh Characteristics						
Domain size	[m]	3500 × 2400	3500 × 2400	8000 × 4500	3800 × 2400	4000 × 4000
Maximum horizontal mesh resolution	[m]	20	20	20	20	20
Number of cells	[-]	873 136	873 136	3 715 666	873 136	1 696 842

Table 2: Characteristics of the numerical modelling by GPI.

Method Ramboll

For the calculation of the LiDAR corrections, Ramboll applied the model Meteodyn WT. This state-of-the-art model solves the three-dimensional Reynolds-averaged Navier-Stokes equations in high spatial resolution. The orography and the surface roughness enter as boundary conditions and turbulence is implemented with a k-ε-model. Stability and the effect of forests are considered.

The simulations of the wind conditions at the considered sites consider the effect of complex terrain on the momentum balance not only by surface roughness, but also by including drag over the entire vertical extent of the forest. Furthermore, forest is included as a source term in the equation of the turbulent kinetic energy. Forested areas and similar structures are modelled by their horizontal extent, height, and density in the CFD-model. This CFD-model can simulate the vicinity of the LiDARs with a higher spatial resolution in order to obtain the direction-dependent corrections. Directional speed-up factors have been computed for each point in the calculated grid. Table 3 shows the parameter Ramboll used for these simulations.

	Units	Site A	Site B	Site C	Site D	Site E	Site A-E, alternative
Modelling specs							
Modelling approach	-	CFD					~
Flow model	-	Meteodyn					~
Correction approach	-	Software-immanent					~
Forest modelling approach	-	Dissipative model					~
Buffer layer´s height	[m]	15			20		~
Tree height/roughness ratio	[-]	20			25		~
Forest density	-	Normal					~
Stability considered	-	Class 4					Class 7
Input data							
Roughness input data	-	CLC-2018					~
Elevation data	-	Austrian Elevation Service, DGM 10					~
Mesh Characteristics							
Domain Radius	[m]	10 000					~
Horizontal resolution at lidar	[m]	8					~
Horizontal expansion coeff.	[-]	1.1					~
Number of cells	[-]	873 956	700 284	625 300	1 392 930		~

Table 3: Characteristics of the numerical modelling by Ramboll.

Method Vaisala

Vaisala contributed two variants of two modeling types. The first method is Flow Complexity Recognition (FCR) WindCube's embedded correction method, commercialized in 2012. This method is based on the SWIFT mass-conservation CFD model, developed by ARIA Technologies. The flow field boundary conditions are set by the measured (uncorrected) profiles of the u_x and u_y components, extrapolated to the surface and boundary top. For initialization, u_z is fixed at 0 m/s. These profiles are used for the whole X-Y domain. Next, the corrected u_x, u_y, and u_z components are derived through the method of Lagrange multipliers, constrained by the incompressibility condition ($\nabla \cdot \vec{\mathrm{u}} = 0$), and the square of the distance to the original u_x, u_y, and u_z profiles.

A variant of FCR that includes a forest treatment ("FCR Canopy") is also included. Forestry (and other surface variations) are parametrized via a uniform characteristic height, below which, the wind profile follows an exponential profile.

The second contributions from Vaisala use the Meteodyn WT CFD correction, described above in the Ramboll section. In the Vaisala contribution, the stability is varied for each 10-minute period according the best fit of the normalized wind profile to the modeled profiles provided with each stability class.

A variant is provided for Sites A, B, and C that uses the same Meteodyn WT model and stability selection method, but with WindCube data reprocessed with hybrid wind field reconstruction. This is a ⅔$^{\text{rds}}$ - ⅓$^{\text{rd}}$ blend of scalar and vector wind field reconstruction. This method has been shown in flat terrain to reduce LiDAR sensitivities to turbulence.

Table 4 and Table 5 summarize the main modelling characteristics used by Vaisala.

	Units	Site A	Site B	Site C	Site D	Site E	Site A-E, alternative
Modelling specs							
Modelling approach	-	Mass conservation					
Flow model	-	SWIFT					
Correction approach	-	Standard correction of flow curvature only					
Forest modelling approach	-	None					Specific forest model including displacement height and forest density
Stability considered	-	Correction is based on 10-minute wind profile: some stability effects accounted for via coherence between simulated flow and LiDAR wind profile					
Input data							
Roughness input data	-	Corine land cover					
Elevation data	-	SRTM - 90 meters - downscaled to 10 meters with internal algorithm					
Mesh Characteristics							
Domain size	[m]	1000 × 1000					
Maximum horizontal mesh resolution	[m]	N/A					
Number of cells	[-]	10 000					

Table 4: Characteristics of the numerical modelling by Vaisala, FCR and FCR Canopy.

	Units	Site A	Site B	Site C	Site D	Site E	Site A-C, alternative
Modelling specs							
Modelling approach	-	RANS CFD					
Flow model	-	Meteodyn WT					
Correction approach	-	Angle and wind speed correction					Hybrid WFR applied to WindCube data
Stability considered	-	Class 0 – 7 chosen based on best fit to wind profile					

Table 5: Characteristics of the numerical modelling by Vaisala and Meteodyn

Method Deutsche WindGuard

The correction approach applied by Deutsche WindGuard is based upon an inhouse developed correction algorithm, taking into account the wind LiDAR’s reconstruction algorithm, in conjunction with results from the high-resolution Computational Fluid Dynamics (CFD) model OpenFOAM which is applied via the CFD toolbox ZephyTOOLS by ZephyScience. OpenFOAM provides a numerical solution based on Reynolds-Averaged Navier-Stokes Equations with k-ε or k-ω-SST turbulence model, which are widely applied and validated models describing turbulent transport and dissipation. One main advantage of OpenFOAM, in comparison with most other CFD codes applied for wind energy purposes, is the ability to use an unstructured calculation grid, permitting the resolution of complex topographies more efficiently and at higher resolution in the relevant areas. This is an important aspect, as sufficiently high resolution can be seen as a precondition for accurate flow simulation.

The wind LiDAR-measured horizontal wind speed at the LiDAR's location is derived from the radial velocities measured along the laser beams (Figure 1), taking into account the device specific reconstruction algorithm. In complex terrain, where the assumption of homogeneous flow conditions within the scan/beam volume is expected to be not valid, the radial velocities (i.e. line-of-sight wind speed components along the beam direction) at the center of the probe volumes are modelled in OpenFOAM. Based upon the modelled line-of-sight (LoS) components, the horizontal wind speed at the LiDAR position is reconstructed ($u_{\mathrm{h,\,LoS}}$) and compared to the CFD-modelled horizontal wind speed at the LiDAR position ($u_{\mathrm{h,\,modelled}}$). The correction factor, calculated for each 10° at the calculation domain's inlet, is defined as

$$LCF = \frac{u_{\mathrm{h,\,modelled}}}{u_{\mathrm{h,\,LoS}}}$$

where LCF is the LiDAR correction factor to be applied to raw wind LiDAR measurement wind speed data, $u_{\mathrm{h,\,modelled}}$ is the horizontal Wind Speed at LiDAR position based upon CFD-modelling results, and $u_{\mathrm{h,\,LoS}}$ is the horizontal wind speed at LiDAR position based upon reconstructed, CFD-modelled LoS wind speed components.

	Units	Site A	Site B	Site C	Site D	Site E	Site A-E, alternative
Modelling specs							
Modelling approach	-	RANS steady-state					~
Flow model	-	OpenFOAM					~
Correction approach	-	Inhouse					~
Forest modelling approach	-	by roughness length					~
Stability considered	-	No					~
Input data							
Roughness input data	-	GLC-2017					~
Elevation data	-	Austrian Elevation Service					SRTM-1 (30m)
Mesh Characteristics							
Domain diameter	[m]	24 828					23 000
Maximum horizontal mesh resolution	[m]	12					10
Number of cells	[-]	8 975 465	9 113 280	8 373 420	9 005 620	8 949 950	11 892 316

Table 6: Characteristics of the numerical modelling by WindGuard.

Geometrical correction approach

In addition to modelling-based correction approaches, a geometrical correction approach has been applied to the LiDAR data from the five sites under consideration:

To get a broader picture of the different correction methods, a rather simple trigonometric approach has also been tested in addition to flow modelling. A wind LiDAR measures the radial wind speed in along the beams (line-of-sight wind speeds) ($u_{N\|}$, $u_{E\|}$, $u_{S\|}$, $u_{W\|}$). Since the LiDAR beams are inclined from the vertical by an angle φ, the horizontal (u_x and u_y) and the vertical (u_z) components of the wind vector are related to the measured, line-of-sight Doppler wind speeds (parallel to the beam, denoted with || in subscript) as:

$$u_{N\|} = u_y \sin\varphi + u_z \cos\varphi$$

$$u_{E\|} = u_x \sin\varphi + u_z \cos\varphi$$

$$u_{S\|} = -u_y \sin\varphi + u_z \cos\varphi$$

$$u_{W\|} = -u_x \sin\varphi + u_z \cos\varphi$$

Solving for the wind speed components yields the wind speed components as measured by a LiDAR:

$$u_{x\ \mathrm{LiDAR}} = \frac{u_{E\|} - u_{W\|}}{2\sin\varphi}$$

$$u_{y\ \mathrm{LiDAR}} = \frac{u_{N\|} - u_{S\|}}{2\sin\varphi}$$

$$u_{z\ \mathrm{LiDAR}} = \frac{u_{E\|} + u_{W\|}}{2\cos\varphi} \quad \text{or} \quad u_{z\ \mathrm{LiDAR}} = \frac{u_{N\|} + u_{S\|}}{2\cos\varphi}$$

Calculating u_x and u_y in this scheme does not take the u_z component into account, whereas the vertical component of the wind speed u_z can be calculated from either pair of opposing beams (or from a combination of all four beams).

In complex terrain, the wind speed vector $\vec{u}$ can have a significant component in vertical direction that in general will be different from on beam to the other. Assuming, following (Bingöl, Mann, & Foussekis, 2008), that the vertical component of the wind speed u_z varies linearly in the x direction, i.e.

$$u_z = \alpha \cdot x + const.$$

and evaluating $u_{x\ \mathrm{LiDAR}}$ as outlined above would introduce a deviation between actual an measured wind

$$u_{x\ \mathrm{LiDAR}} = u_x + \alpha \cdot H$$

with H being the LiDAR’s measurement height.

In the geometrical correction approach used in this study, it has been attempted to estimate the vertical wind speed’s gradient α by comparing the four corner beam’s measurements with the vertical wind speed $u_{z\ \mathrm{vert.}}$ measured by the vertical (5th) beam.

$$\alpha = \frac{du_z}{dx} = \frac{u_{z\ N,E,S,W} - u_{z\ \mathrm{vert.}}}{x}$$

With estimates of the gradient of the vertical wind speed in x and y direction, the corrections for the LiDAR windspeed (i.e. the difference $u_x - u_{x\ \mathrm{LiDAR}}$) it is then obtained as $-\alpha \cdot H$.

4. Results

The description of the results in this section is structured in four thematic subsections as follows: First, in Section 4.1, a comparison and statistics of measured wind speeds by the LiDAR (uncorrected) and the met mast anemometer allows a quantification and characterization of the measurement errors and uncertainties at the five considered sites. In Section 4.2, characteristics for the flow conditions at the five sites are calculated from the measured wind speed components at different measurement heights. Characteristics for the terrain complexity are evaluated in Section 4.3 as a possible basis for the correlation of the observed measurement errors with properties of the terrain. Finally, Section 4.4 discusses the terrain complexity correction factors as calculated with the various methods.

4.1. Comparison of LiDAR and Met mast data

The uncorrected deviations between the wind LiDAR and met mast measurements for the five sites A to E are illustrated in Figure 7 to Figure 11. For very low wind speeds, the relative measurement errors (i.e. $0.5 \cdot (ws_{LiDAR} - ws_{Met\ Mast})/(ws_{LiDAR} + ws_{Met\ Mast})$) may become very large. As the accuracy at low wind speeds is usually not relevant in wind energy applications, wind speeds below 2.5 m/s are not included in Figure 7 to Figure 11. For binning by wind direction, the wind direction as recorded by the wind LiDAR has been used, being more significant for the present analysis than a wind vane on the met mast.

In the upper left corner of Figure 7 to Figure 11, some important scalar measures for the deviation of LiDAR and met-mast anemometry are displayed. The definitions for these quantities are given below. Thereby u refers to the wind speed, $i = 1 \dots N$ denote the 10-minute measurement intervals, $j = 1 \dots 36$ denote the bins in wind direction with a bin-width of 10°, and N_j is the number of 10-minute samples in wind direction bin j.

$$\text{"LiDAR - MetMast"} = \frac{1}{N}\sum_{i=1}^{N} u_{\text{LiDAR 10}'} - u_{\text{Met Mast 10}'}$$

$$\text{"mean LiDAR/MetMast"} = \frac{1}{N}\sum_{i=1}^{N} \frac{u_{\text{LiDAR 10}'}}{u_{\text{Met Mast 10}'}}$$

$$\text{"range LiDAR/Met Mast"} = \max_{j=1\dots36}\left(\frac{1}{N_j}\sum_{i=1}^{N_j} \frac{u_{\text{LiDAR 10}'}}{u_{\text{Met Mast 10}'}}\right) - \min_{j=1\dots36}\left(\frac{1}{N_j}\sum_{i=1}^{N_j} \frac{u_{\text{LiDAR 10}'}}{u_{\text{Met Mast 10}'}}\right)$$

"mean interquartile range” refers to the average height of the solid blue boxes in the box plots for the 36 wind direction bins, the range of the 25th and 75th percentiles of the error distribution.

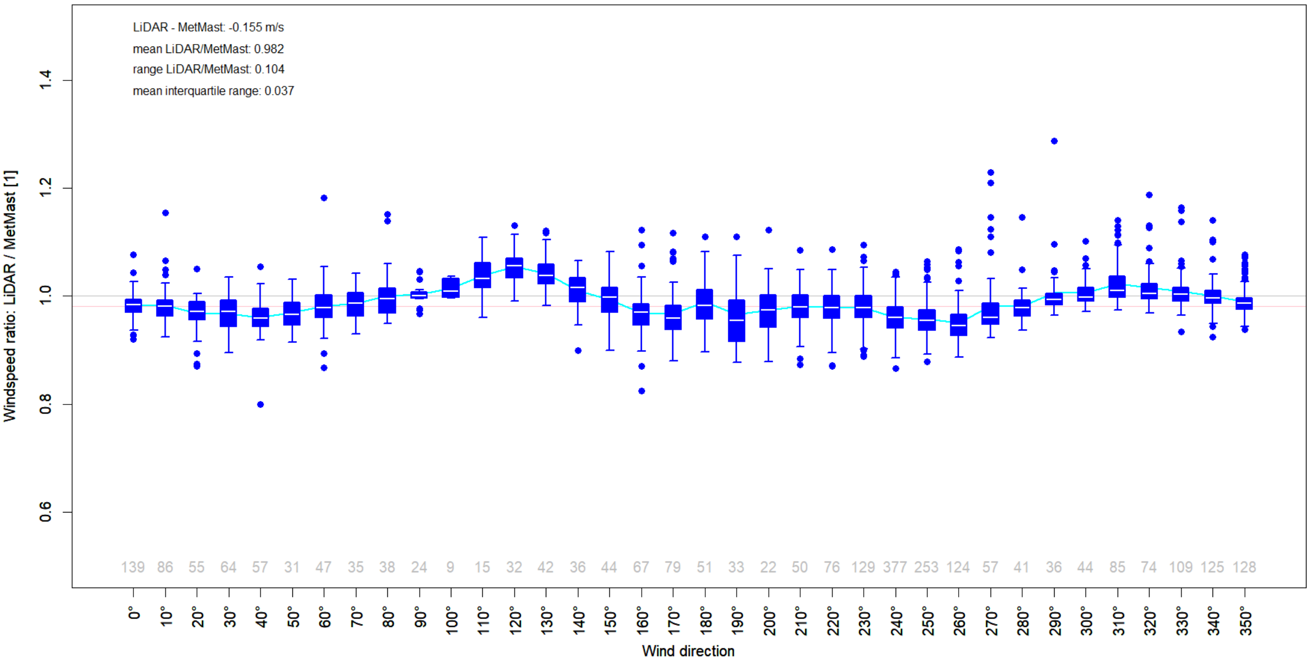

Figure 7: Ratio between LiDAR measurement and met mast measurement for Site A. For each wind direction bin, the distribution of the recorded ratio of LiDAR and met mast wind speeds is illustrated as a box plot. Thereby, the solid blue box illustrates the interquartile range, i.e. the range between the 25% and the 75% quantile. The white horizontal maker in the box gives the median of the distribution. The whiskers above and below the box show the range of data points within a maximum distance of 1.5 times the interquartile range. Data points beyond the 1.5 times the interquartile range are considered as outliers and are included separately as blue dots. The gray numbers above the horizontal axis give the number of data samples in each bin. The

mean deviation per bin is shown as light blue line. The light red line gives the deviation averaged for all directions.

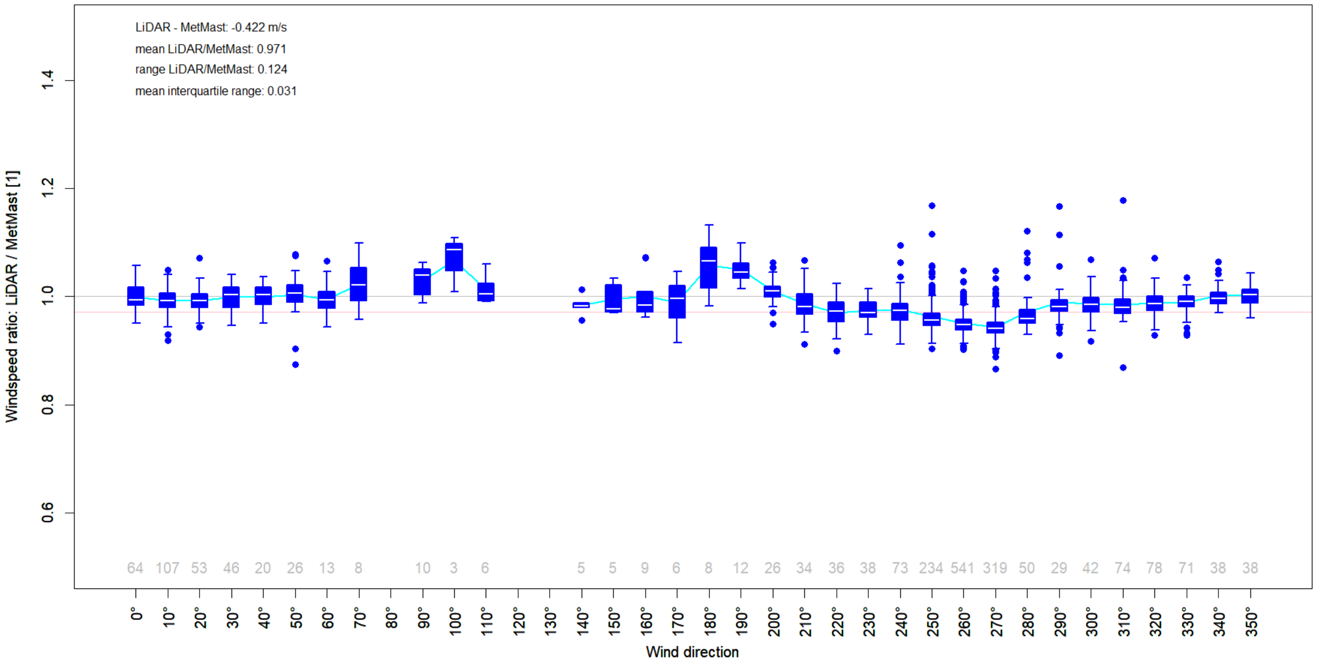

Figure 8: Ratio between LiDAR measurement and met mast measurement for Site B. For the interpretation of symbols and lines see caption to Figure 7.

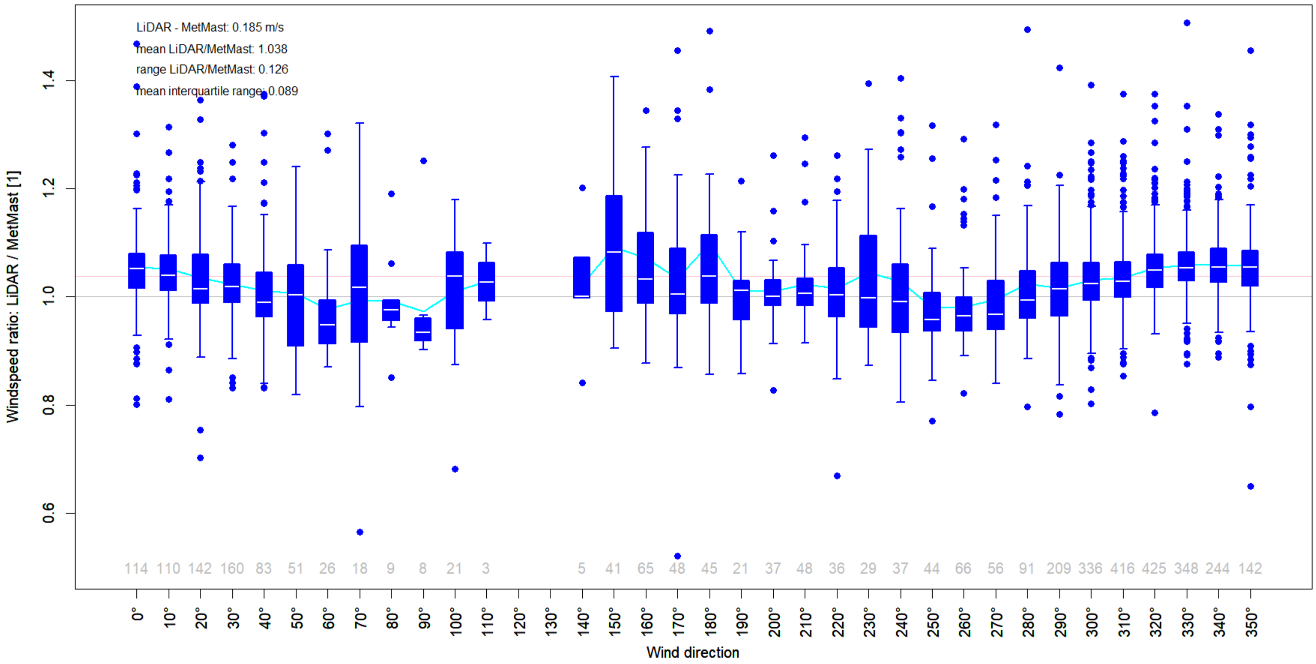

Figure 9: Ratio between LiDAR measurement and met mast measurement for Site C. For the interpretation of symbols and lines see caption to Figure 7.

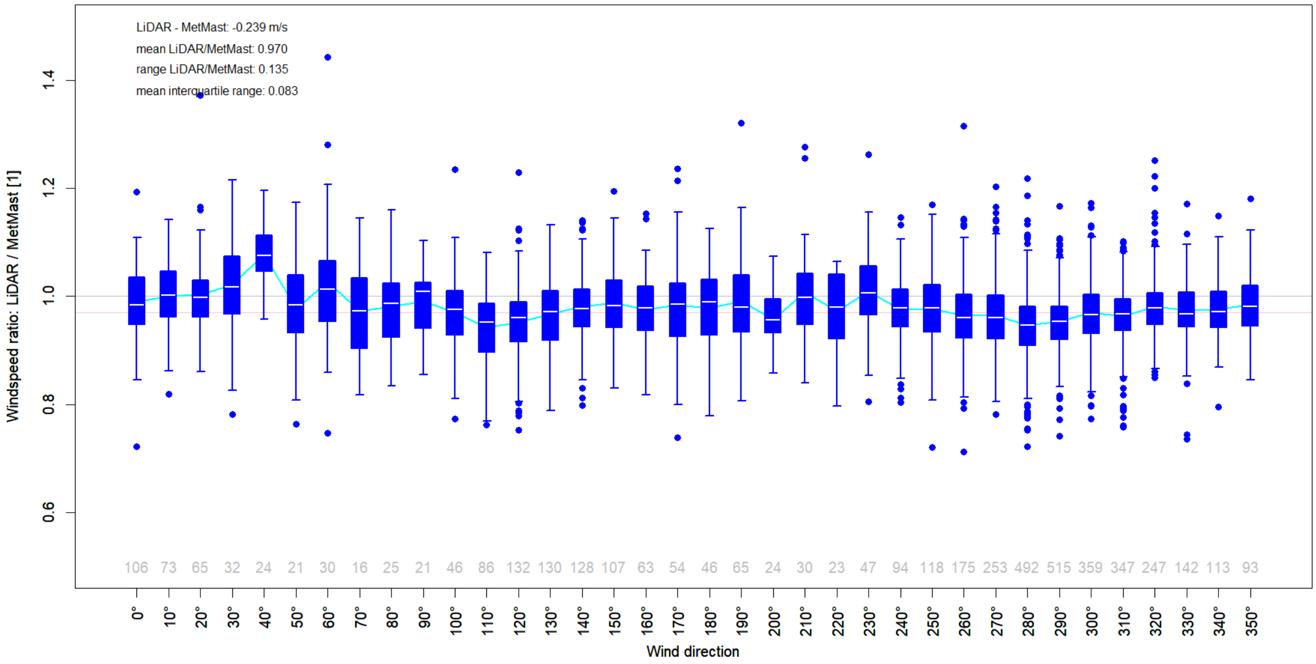

Figure 10: Ratio between LiDAR measurement and met mast measurement for Site D. For the interpretation of symbols and lines see caption to Figure 7.

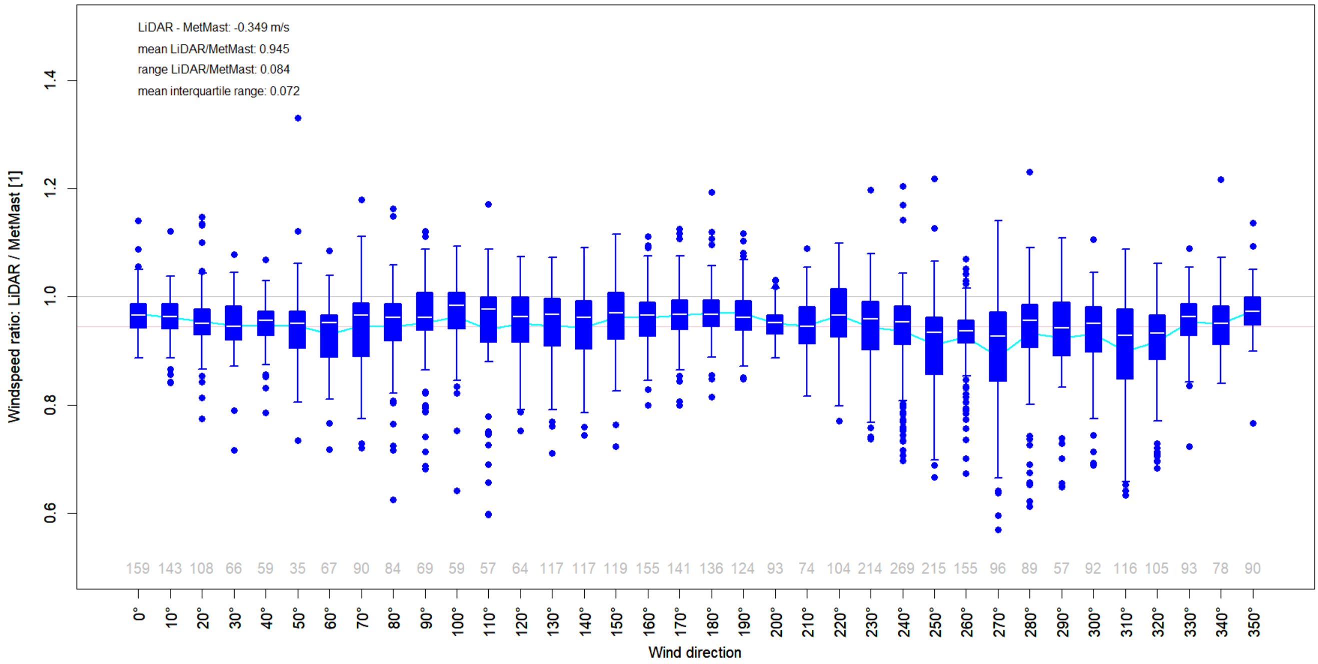

Figure 11: Ratio between LiDAR measurement and met mast measurement for Site E. For the interpretation of symbols and lines see caption to Figure 7.

Some general observations from this comparison of LiDAR and met mast wind speeds are:

- There is a systematic variation of the wind speed ratio for different wind directions that can be explained from the different effect of the terrain and different complex flow condition depending on the direction of flow.
- The ratio of the average LiDAR wind speed to the average met mast wind speed alone (i.e. the quantity "mean LiDAR/MetMast") is insufficient to assess the overall differences between the measurements and the fidelity of the wind LiDAR measurement. Significant deviations in individual wind directions may cancel out by chance, when summing up over all wind directions.
- The deviation between LiDAR and met mast in a particular wind direction is not a simple scaling law with a constant factor between the LiDAR and met mast wind speed but a distribution with a definite width. Position, width and shape of these distributions depend on the site and on the wind direction and exhibit a large variability as indicated by the individual box plots in Figure 7 to Figure 11. These distributions reflect measurement errors (both of the cup anemometer and the LiDAR) as well as variations in the flow.
- In addition to the systematic, wind-direction dependent deviation of the mean wind speeds (position of the distribution, first point of this list), there is also a systematic dependency of the width of the distribution with the wind direction. This suggests an influence of the terrain through flow characteristics such as turbulence, shear, and flow inclination.
- The comparisons between LiDAR and met mast data were all characterized by a large component of stochastic variability (“noise”). In two of the five met mast measurements considered in this study, 3D ultrasonic anemometers were deployed at a level somewhat below the cup anemometer in the mast top. In these cases, comparison between the cup and the ultrasonic anemometer did not exhibit this high level of stochastic deviation. This suggests that anemometer uncertainty is of lesser importance here and that the observed stochastic variability is in fact correlated to flow inhomogeneity and variability.

Table 7 compiles the four scalar measures for the deviation of LiDAR and met-mast data defined earlier in this section. These are the same as those displayed in the upper left corners of Figure 7 to Figure 11.

	Site A	Site B	Site C	Site D	Site E
Reference height	85.5 m	85.5 m	85.5 m	52.5 m	52.5 m
LiDAR – MetMast [m/s]	-0.155 m/s	-0.422 m/s	0.185 m/s	-0.239 m/s	-0.349 m/s
mean LiDAR/MetMast [1]	0.982	0.971	1.038	0.970	0.945
range LiDAR/Met Mast [1]	0.104	0.124	0.126	0.135	0.084
mean interquartile range [1]	0.037	0.031	0.089	0.083	0.072

Table 7: Statistics of the deviations between LiDAR and met mast measurements for the five sites A to E.

Comparison of turbulence intensities obtained with LiDAR and met mast

Wind LiDAR measurements yield systematically higher turbulence intensities (TI) than the cup anemometer measurements on the met mast (see Table 8). This observation is most likely connected to the respective measurement principles of LiDAR devices and cup anemometers. Consistent and comparable determination of turbulence intensities with LiDAR are an important topic and the subject of ongoing research activities (e.g. TI Working group of IEA Wind TCP Task 52). It is however, not in the scope of the present analysis.

	Site A	Site B	Site C	Site D	Site E
Reference height	85.5 m	85.5 m	85.5 m	52.5 m	52.5 m
LiDAR mean TI at reference height	0.155	0.134	0.192	0.206	0.156
Met mast mean TI at reference height	0.121	0.114	0.158	0.162	0.114

Table 8: Comparison of turbulence intensities from LiDAR and met mast measurements for the five sites. The numbers are based on time intervals with parallel availability of LiDAR and met-mast data. A lower wind speed cut-off of 2.5 m/s has been employed.

Atmospheric Stability

Atmospheric stability has an important effect on wind shear and on the vertical profile of the wind and thus also affects LiDAR measurements and LiDAR correction techniques. Figure 13 illustrates the flow profile for different atmospheric stabilities in numerical models calculated with RIAM-COMPACT.

Table 9 shows atmospheric stabilities for the five sites in this study as determined from the flow models, which assumed neutral and stable conditions. A vortex time series served as a source. The evaluation period is the same as for the LiDAR measurements.

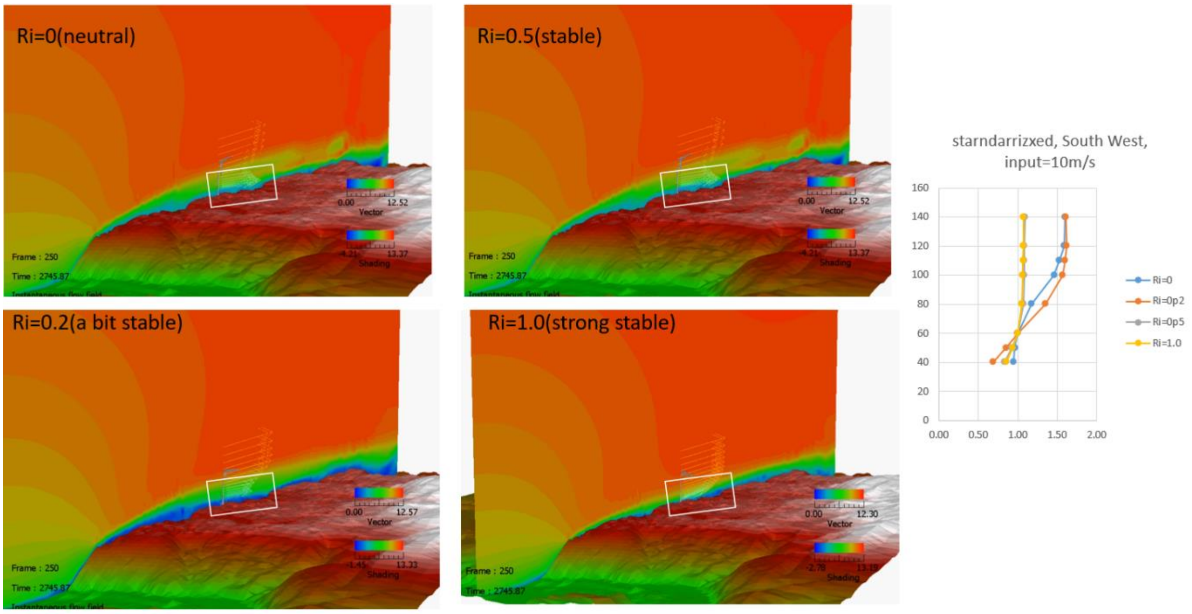

Figure 12: Models with different atmospheric stability for a Japanese site. The panel on the right side shows the corresponding wind profiles. The models have been calculated with RIAM-COMPACT.

	Site A	Site B	Site C	Site D	Site E
Ri number	0.210	0.140	0.090	-0.030	0.000
Atmospheric stability	stable	stable	a bit stable	neutral	neutral

Table 9: Richardson number at each site according to the definitions of (Leelőssy, et al., 2014).

4.2. Flow characteristics in LiDAR data

Compared to a traditional cup anemometer, which only gives a single number for the wind speed, a vertical profiling wind LiDAR records much more information about the flow. Hence, one way to characterize the flow at a site, is to use this information available from the LiDAR measurement, i.e., data at several measurement heights for the horizontal and vertical wind speed components, the wind direction, standard deviations (turbulence intensities), signal-to-noise ratio, etc.

Wind shear

Table 10 gives the wind shear exponent α for the five sites, as fitted to the 10-min averaged shear profiles. Data with wind speeds (at reference height) below 2.5 m/s have been excluded. In general, there is only a slight, if any, variation of the wind shear exponent α with the time of the day. Thermal stratification thus seems to play a minor role only. There is also no prominent variation of wind shear with the direction of the wind.

There is however a significant variation from site to site, with Site E on average showing almost no wind gradient. One explanation for this observation could be a local compression of the wind at the peak close to the LiDAR's position at Site E, counteracting a background wind shear profile.

	Site A	Site B	Site C	Site D	Site E
5% quantile of wind shear exponent α	-0.26	-0.07	-0.09	-0.17	-0.35
Mean wind shear exponent α	0.19	0.23	0.22	0.12	-0.01
95% quantile of wind shear exponent α	0.57	0.60	0.56	0.44	0.32

Table 10: Wind shear expressed as wind shear exponent α for the five sites. The exponent has been fitted using data from all measurement heights as availability permitted. Only data with wind speeds above 2.5 m/s (at reference height) have been taken into account.

Turbulence intensity

The mean turbulence intensities (TI) at the five sites, as well as the width of the distribution of the turbulence intensities, are summarized in Table 11. Compared to Table 8, this includes all data points available, without consideration of parallel met-mast data and without a lower wind speed cut-off.

The turbulence intensities generally decrease, as expected, for greater measurement height. A notable exception is Site E, where TI rises again somewhat at heights above 100 m. A correlation of TI with the time of the day can be observed to a varying degree at all five sites.

	Site A	Site B	Site C	Site D	Site E
Reference height	85.5 m	85.5 m	85.5 m	52.5 m	52.5 m
5% quantile of turbulence intensity	0.06	0.05	0.07	0.08	0.05
Mean turbulence intensity	0.19	0.16	0.22	0.23	0.19
95% quantile of turbulence intensity	0.44	0.35	0.46	0.46	0.45

Table 11: Turbulence intensity for the five sites at reference height.

Vertical inflow angle

All sites in this study are located in complex terrain and thus exhibit, depending on the terrain profile in the corresponding wind direction, vertical wind components and wind vectors that are inclined from the horizontal plane. Among the five sites, Site C is distinct in being located on a slope (see Figure 4). This is correspondingly reflected in the illustration of the inflow angle as a function of wind direction in Figure 13, which shows a range of vertical inflow angles roughly between -15° and +15°. For greater measurement heights, the effect of the terrain profile decreases, leading to smaller extreme values of the vertical inflow angle.

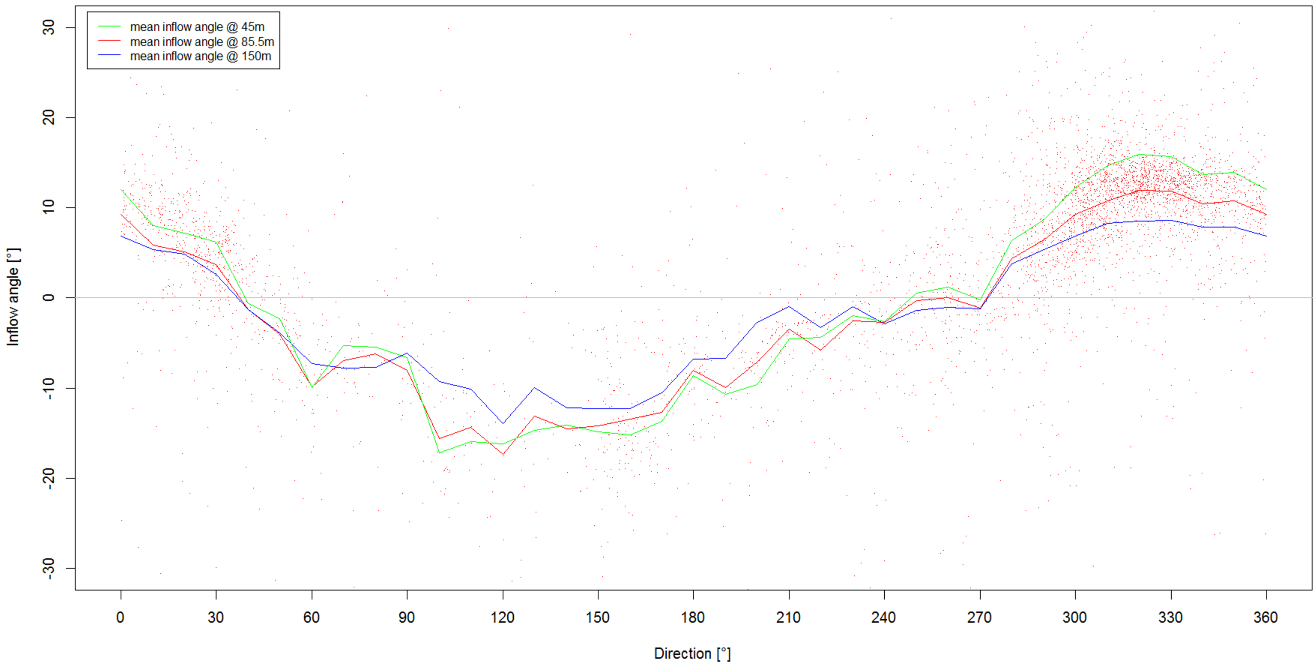

Figure 13: Vertical inflow angle as a function of wind direction for Site C at three different heights. Inflow angles for all data points at a height of 85.5 m are included as red dots.

A summary of statistics of the vertical inflow angle for all five considered sites is given in Table 12. Results have been compiled at two levels; 52.5 m and 85.5 m. Vertical interpolation of the wind data has been used to calculate the inflow angles at the two levels. No low wind speed cut-off has been used. The highest inflow angles are obtained for Site C, for the reason mentioned above. As to be expected, the inflow angles in Figure 13 decrease with greater measurement height. In general, this observation is valid for all five sites under consideration.

	Site A	Site B	Site C	Site D	Site E
Mean abs. inflow angle for all direction bins at 52.5 m	2.2°	5.9°	8.7°	2.8°	1.5°
Max. inflow angle for all direction bins at 52.5 m	+1.2°	+2.0°	+14.6°	+2.4°	+2.2°
Min. inflow angle for all direction bins at 52.5 m	-10.2°	-15.9°	-16.2°	-6.9°	-4.3°
Mean abs. inflow angle for all direction bins at 85.5 m	2.4°	5.4°	8.1°	2.8°	2.0°
Max. inflow angle for all direction bins at 85.5 m	+0.6°	+1.1°	+12.0°	+2.8°	+4.0°
Min. inflow angle for all direction bins at 85.5 m	-7.4°	-11.9°	-17.3°	-7.6°	-5.0°

Table 12: Statistics of inflow angles for Sites A to E. The data points have been binned in wind direction with a bin-with of 10°. For these bin-averaged inflow angles, maximum, minimum and mean of all 36 bins are given in the table for two different heights. Vertical interpolation of wind speeds based on 10-min data has been used to obtain inflow angles at the two reference heights of 52.5 m and 85.5 m.

4.3. Terrain characterization

The most direct way to assess the complexity of a site, is the use of terrain data; such as digital terrain models, data on surface roughness and vegetation height, and position and character of obstacles. Such information will usually be available from maps or aerial photography. Hence, an assessment of the complexity of a site through terrain characterization, already in the planning phase of a measurement campaign, is particularly useful to estimate the suitability of a site for a wind LiDAR measurement and/or LiDAR correction.

An important parameter when characterizing the terrain for a wind LiDAR measurement site is the extent of the area to be taken into account in the characterization. Terrain close to the measurement position will usually have the largest effect on the flow conditions, while more remote terrain features will have a lesser influence. Although, there will likely be exceptions, where remote obstacles have a very significant effect on the flow conditions.

It is thus not easy to define a generally valid “effect radius” around a measurement position for the area to be taken into account in a terrain characterization. The geometry of the problem suggest the measurement height to be a useful scale length. Since a ground based LiDAR measurement will usually record wind speeds at several heights, one typical height or height of interest needs to be defined. This height is here referred to as “reference height” and subsequently denoted as H. Based on that, four different evaluation radii (2·H, 3·H, 5·H and 10·H) around the measurement positions are explored for terrain characterizations to assess ground based LiDAR measurements.

For the five sites A to E considered in this study, the height of the co-located met mast as the main “height-of-interest” is taken as the reference height.

Slopes

One way to assess the complexity of the terrain is to investigate the slopes of the terrain. Calculating the components of the local slope $\left(\frac{\partial z}{\partial x}\right)_i$ and $\left(\frac{\partial z}{\partial y}\right)_i$ at a position i (where z is the elevation and x and y are the coordinate directions), requires a spatial length scale (Δx or Δy, respectively) for discretization. In many implementations, this will be identical to the mesh size of the digital terrain model. The calculated slopes may critically depend on this length scale, defining the separation between terrain contour and terrain roughness.

In devising a measure for the terrain complexity based on terrain slopes, we therefore use the average of the slope in the coordinate directions. Thereby slopes on smaller length scales than the effect radius cancel out, yielding an average slope for the total of the considered area:

$$\text{"abs(mean(slope))"} = \sqrt{\left(\frac{1}{N}\sum_{i=1}^{N}\left(\frac{\partial z}{\partial x}\right)_i\right)^2 + \left(\frac{1}{N}\sum_{i=1}^{N}\left(\frac{\partial z}{\partial y}\right)_i\right)^2}$$

Here, N is the number of grid points of the digital terrain model within the considered radius. The results for this average slope complexity measure for the Sites A to E are given in Table 13 for evaluation radii of 2·H, 3·H, 5·H and 10·H.

	Site A	Site B	Site C	Site D	Site E
Reference height H	85.5 m	85.5 m	85.5 m	52.5 m	52.5 m
abs(mean(slope)) for 2·H	4.7°	7.1°	19.6°	2.6°	1.4°
abs(mean(slope)) for 3·H	4.2°	7.2°	17.9°	3.7°	1.7°
abs(mean(slope)) for 5·H	3.4°	6.1°	12.5°	7.2°	1.1°
abs(mean(slope)) for 10·H	4.7°	5.0°	8.3°	8.0°	1.7°

Table 13: Average slopes of the terrain around the measurement positions at the five sites with evaluation radii between 2 times and 10 times the reference height H.

Elevation

The most direct way to assess terrain complexity is statistics of the individual data points for terrain elevation. One possible measure for terrain complexity is the range of elevation in the assumed effect radius for the flow conditions at a measurement position. To minimize the dependency on the numerical representation of the terrain (grid orientation and resolution), extreme elevations are evaluated as the 5% quantile and the 95% quantile instead of plain minimum and maximum values. Table 14 gives both the 5% and the 95% quantiles as well as the elevation range (95% quantile – 5% quantile) for all five sites and for evaluation radii between 2·H and 10·H.

	Site A	**Site B**	**Site C**	**Site D**	**Site E**
Reference height H	85.5 m	85.5 m	85.5 m	52.5 m	52.5 m
Elevation range [m] and (95%/5%) quantiles for 2·H	38.8 (+18.7/-20.1)	38.1 (+18.8/-19.3)	103.4 (+51.0/-52.4)	9.7 (+3.3/-6.39)	9.9 (+3.9/-6.0)
Elevation range [m] and (95%/5%) quantiles for 3·H	59.2 (+27.6/-31.6)	63.3 (+27.1/-36.2)	145.3 (+74.3/-71)	20.1 (+6.9/-13.2)	19.7 (+8.2/-11.5)
Elevation range [m] and (95%/5%) quantiles for 5·H	99.5 (+42.9/-56.6)	112.3 (+44.3/-68.0)	202.6 (+107.1/-95.5)	56.3 (+18.4/-37.9)	42.0 (+19.2/-22.8)
Elevation range [m] and (95%/5%) quantiles for 10·H	175.8 (+74.4/-101.4)	210.7 (+81.8/-128.9)	336.7 (+181.4/-155.3)	164.2 (+57.4/-106.8)	123.8 (+54.7/-69.1)

Table 14: Elevation range for Sites A to E defined as difference between the 95% quantile and the 5% quantile within evaluation radii between 2 times and 10 times the reference height H. The 95% and the 5% quantiles are given in brackets. All elevations are given relative to the terrain elevation at the measurement position. Units are Meters.

Terrain curvature

Curvature of the flow lines of the wind can cause systematic errors of ground-based LiDAR measurements (see scheme in Figure 1). On the presumption, that the wind, to some degree, follows the contour of the terrain, the curvature of the terrain should be a useful indicator for the errors of a LiDAR measurement. To calculate representative curvatures for the LiDAR positions, a set of radials originating at the point of the measurement in 30° steps around the compass have been considered. Curvature radii have then been fitted to the elevation data points along each radial up to a pre-defined distance from the measurement point in units of the reference height H. Table 15 summarizes the mean curvatures along the 12 radials at each site.

	Site A	Site B	Site C	Site D	Site E
Reference height H	85.5 m	85.5 m	85.5 m	52.5 m	52.5 m
mean terrain curvature radius for 2·H	852 m	1642 m	836 m	820 m	838 m
mean terrain curvature radius for 3·H:	1221 m	1612 m	1149 m	1034 m	795 m
mean terrain curvature radius for 5·H	1695 m	1503 m	1363 m	1464 m	906 m
mean terrain curvature radius for 10·H	2869 m	2904 m	2505 m	1834 m	1368 m

Table 15: Terrain curvature radius calculated along radials from measurement position in 30° steps for a distance of 2, 3, 5, and 10 times the reference height H. The numbers in the table give the average curvature radius for all 12 radials at each site.

Site ruggedness index RIX

The site ruggedness index RIX has been developed as a criterion for the applicability of the Software WAsP (Mortensen, Bowen, & Antoniou, 2006) and is based on a value for a critical terrain slope that is interpreted as a threshold for flow separation. Independent from the original Wasp application use case, RIX has since become a generally used measure for the description of the complexity of wind energy sites. The site ruggedness index RIX considers a number of radials originating at the point of interest and evaluates the fraction of length where the slope along these radials exceeds the assumed threshold. For the five sites in this study, values RIX have been calculated using a critical slope of 0.3 and for an evaluation radius of 3500 m. The results are given in Table 16.

	Site A	Site B	Site C	Site D	Site E
Site ruggedness index RIX	0.09	0.13	0.39	0.19	0.14

Table 16: RIX for the five considered sites:

A site ruggedness index RIX larger than zero means, that there are some wind directions where within the considered evaluation radius of 3500 m, flow separation is likely to occur. Hence, according to RIX, all five sites A to E shall be considered to be complex terrain sites.

Complex terrain classification according to IEC 61400-1

Part one of the wind energy standard IEC 61400 (International Electrotechnical Commission, 2019) contains a scheme for the assessment of terrain complexity, based on terrain slopes and terrain variation within certain radii around the point of interest. This is expressed as terrain slope index (TSI) and terrain variation index (TVI), which can be either calculated for a 30° sector or for a 360° circle (added as subscript). Thresholds for both TSI and TVI then define complexity levels (none, L, M, H), whereby the maximum level for all terrain indices defines the complexity classification of a site. The corresponding results for the five sites in this study are summarized in Table 17. Being focused on wind turbine operation, IEC 61400-1 uses rather larger evaluation radii for the assessment of complexity (5·H, 10·H and 20·H), than what is probably relevant for a ground based LiDAR measurements. In IEC61400-1, the meaning of H is the hub height of the wind turbine whereas in the present application, H has been associated with the reference height of the LiDAR measurement.

	Site A	Site B	Site C	Site D	Site E
TSI_{360} for 5·H	6.06° (-)	11.0° (L)	25.4° (H)	9.10° (-)	2.16° (-)
TSI_{30} for 5·H	9.73° (-)	10.4° (L)	13.0° (L)	7.82° (-)	9.96° (-)
TSI_{30} for 10·H	9.13° (-)	9.78° (-)	14.6° (L)	11.4° (L)	13.7° (L)
TSI_{30} for 20·H	6.71° (-)	5.49° (-)	6.16° (-)	8.23° (-)	13.5° (L)
TVI_{360} for 5·H	2.02% (L)	1.80% (-)	2.33% (L)	1.63% (-)	1.62% (-)
TVI_{30} for 5·H	1.47% (-)	1.47% (-)	2.82% (L)	1.59% (-)	0.98% (-)
TVI_{30} for 10·H	1.48% (-)	1.53% (-)	2.76% (L)	2.30% (L)	1.54% (-)
TVI_{30} for 20·H	1.52% (-)	1.88% (-)	3.64% (L)	2.58% (L)	2.09% (L)
Complexity according to IEC61400-1 (L/M/H)	L	L	H	L	L

Table 17: Classification of the terrain complexity according to IEC 61400-1 for Sites A to E. The symbol in brackets gives the classification of the corresponding index. The lowermost line contains the complexity classification of a site, which results as the maximum classification for all indices in a column. According to IEC61400-1 and the assumed reference heights, Sites A, B, D, and E should be considered to have a "low" complexity, whereas Site C is classified as a "highly" complex site.

4.4. Corrected LiDAR data

In this study, eleven different correction methods have been applied to the LiDAR data. However, as assessed through comparison with met mast measurements, none of these eleven variants proved to be entirely successful in calculating consistent and reliable corrections to LiDAR wind speeds. In some instances, good agreement could be achieved from the application of calculated LiDAR corrections. Nevertheless, no correction method was able to deliver a consistent, significant improvement for all five datasets under consideration.

Therefore, in this chapter, we will not give a thorough discussion of the individual corrections, but rather give an overall review of general principles and observations:

As an example of the improvement that a correction scheme can achieve, Figure 14 shows the remaining deviations from the met mast reference wind speed after a correction has been applied to the LiDAR data. For this plot, a good example of correction factors has been chosen from the eleven different variants of corrections that have been calculated for Site A. For comparison, the deviations of the uncorrected LiDAR data from Site A are shown in Figure 7.

In the case illustrated in Figure 7, the correction in mean wind speed gives an over-correction by about 50%, which nevertheless causes in a slight improvement in mean wind speeds (by about 0.08 m/s), compared to the met mast results. Overcorrection appeared to be a general trend for all correction methods involved and at all five sites.

Apart from this slight improvement in mean wind speed, in this example the LiDAR correction also reduced the range of the LiDAR/met mast error for different wind directions, i.e. the undulation of the turquoise line in Figure 7 and Figure 14. Expressed as the quantity $\text{range LiDAR/Met Mast}$, this corresponds to a reduction from 0.104 m/s to 0.074 m/s.

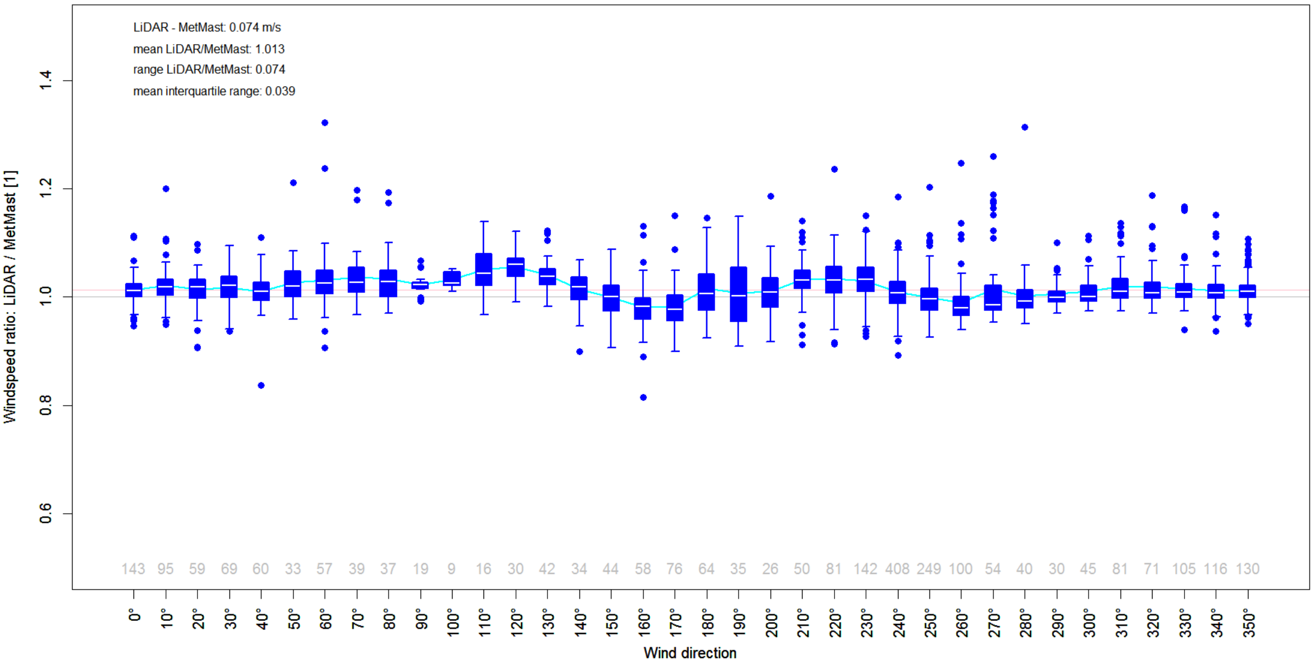

Figure 14: An example of corrected LiDAR wind speeds as compared met mast measurement for Site A. For the interpretation of symbols and lines see caption to Figure 7.

Comparing the different correction methods, there seems to be a basic agreement in the relative amplitude of the correction for different wind directions. To some degree, this in fact removes a part of the undulation of the LiDAR/met mast error (turquoise line in Figure 7 to Figure 11). This is likely connected to a basic agreement among the different correction methods regarding the flow curvature as caused by the terrain contour. Considering the complete set of correction methods in this study, there is nevertheless a very considerable spread between the results of the individual correction methods.

In all correction methods, the calculated corrections were essentially applied as wind direction dependent correction factors to the LiDAR wind speeds. Corrections of that type potentially can adjust the mean wind speed values for all wind direction bins, but will be unable to reduce the scatter in the LiDAR/met mast error within a wind direction bin, i.e. reduce the height of the box plots in Figure 7 to Figure 11.

As mentioned earlier in Section 4.1., the ratio of average wind speeds (i.e. the ratio of two scalar numbers), is not a suitable method to assess the overall differences between measurements, nor the fidelity of measurements or correction methods. Looking at one average number, the mean wind speed for all wind directions in this case, tells little about the ability of a correction method to give reliable and consistent corrections throughout the range of wind conditions and wind directions.

The reason for these inconsistent and dissatisfying results for the LiDAR correction methods probably lies in the terrain and flow complexity at the five sites in this study, which, at least to some extent, exceeds the range of applicability of the methods. There is however still some potential usefulness in the application of such correction methods, as the magnitude of the correction seems to be a good indicator for the range of uncertainty of a ground based LiDAR measurement.

In the TR6 standard (Fördergesellschaft Windenergie und andere Dezentrale Energien (FGW), 2021), it is proposed that the uncertainty assigned to LiDAR flow correction methods is 50% of the correction itself. In the case of this study, we examine a similar statistic for the quantity $\text{mean LiDAR/MetMast}$ (see Section 4.1) evaluated for the corrected dataset, as a function of the original error between the met mast and the uncorrected LiDAR.

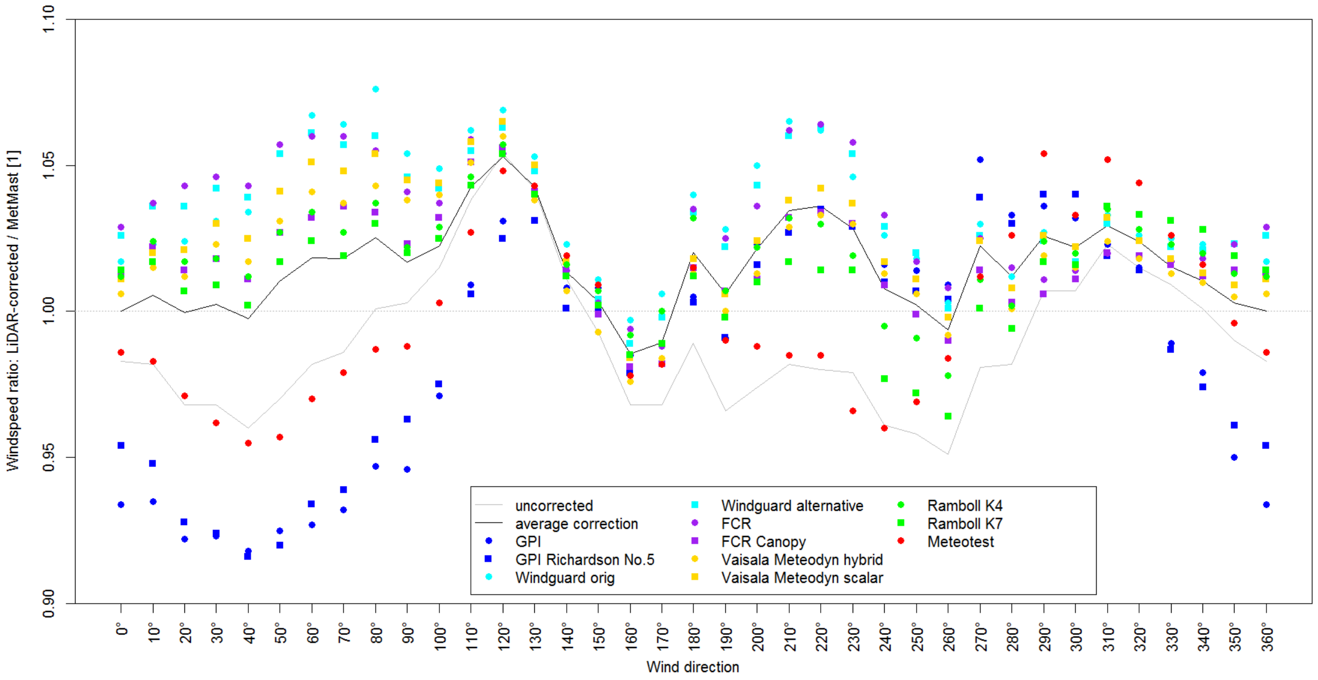

Figure 15: Site A corrected bias as function of direction for various correction methods (colored symbols). Raw error is shown as gray solid line, average of all corrections is shown as black solid line.

Instead of visualizing the site data as a function of wind direction, the quantity $\text{mean LiDAR/MetMast}$ for the LiDAR/met mast deviation is presented in Figure 16 as a function of the original error. For many CFD-based simulations, each wind direction is in fact an independent instance of the flow simulation, so this is a natural way to group the data and examine the skill of the correction methods. Furthermore, this allows aggregate evaluation of correction techniques by pooling together separate sites.

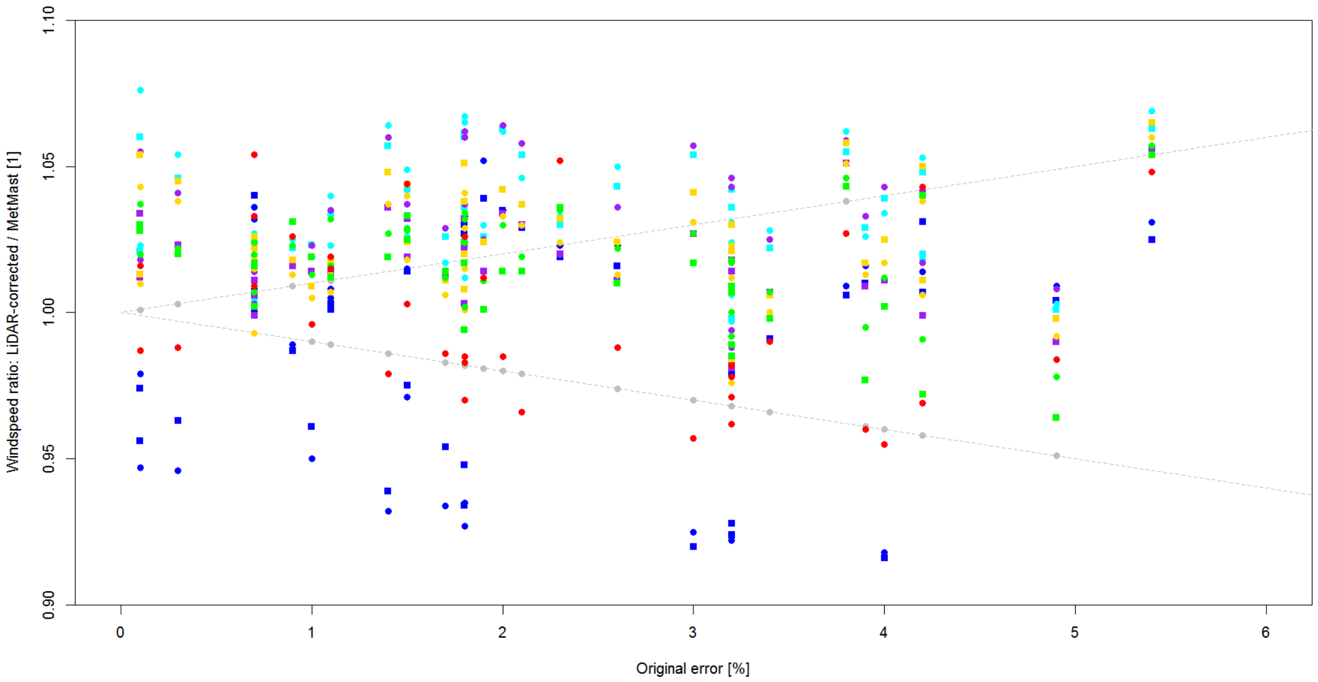

Figure 16: Site A corrected bias as a function of absolute value of original error. Original errors are shown as gray bullets and with a gray dashed line. The meaning of the symbols is the same as in Figure 15.

Figures 16 and 17 show the same data, reshaped to illustrate the skill of models as a function of the original bias. Note that for Site A, the average across all sites is flat, implying that the models have good skill correcting original errors up to 5%. The offset from $y = 0$ implies that there is a consistent high bias in the corrected data, when compared to the co-located met mast. Points that lie inside the gray “original error cone” are improved from the original error by the correction methods, while points outside the original error cone are degraded by the corrections.

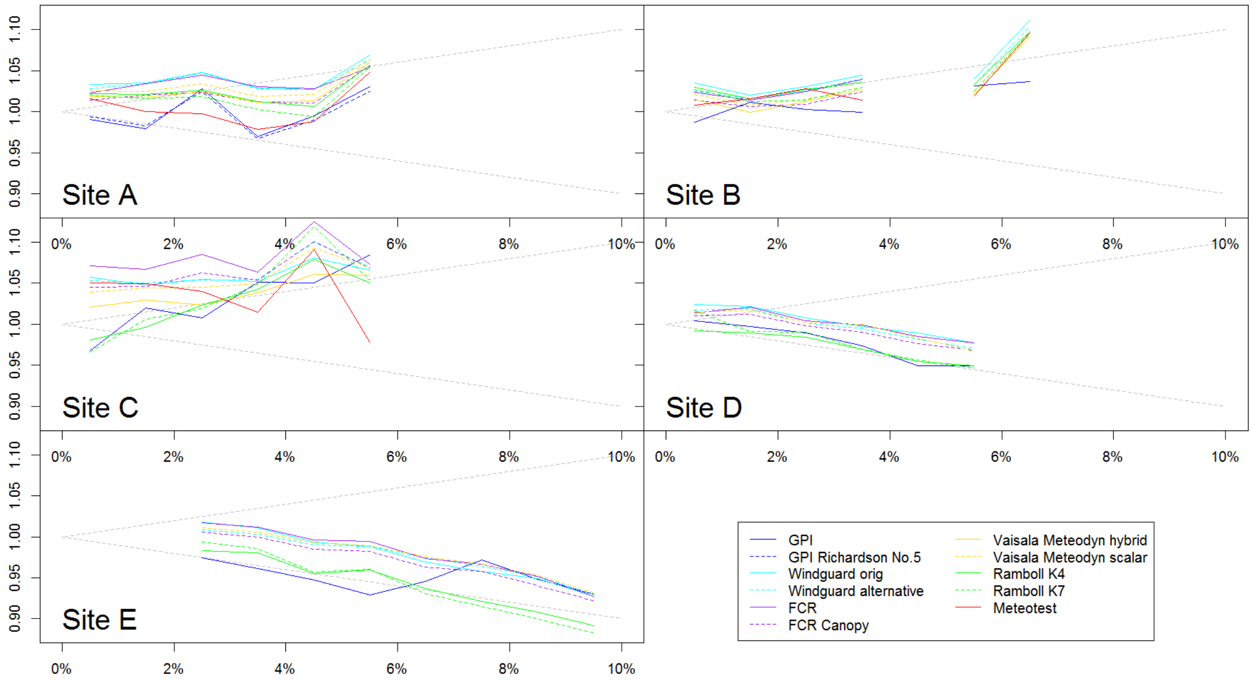

Figure 17: Sites A-E, all correction methods, average corrected bias vs original error. Dashed lines show original error

Figures 18 shows the average corrected biases as a function of the original error, by site. Each data point is the average of the corrected bias for a particular site, for a particular correction method, for all the original biases separated into 1% bins (±0.5%). These graphs show similarities between the correction methods for different sites. Figure 18 shows the same trends for nearly all the correction methods for each of the 5 sites. All of the correction methods struggle with Site C, overpredicting the error and degrading the correlations with the met mast. At Site E, all of the methods underpredict the error and make little improvement to the correlation with the met masts.

5. Understanding LiDAR/Mast Deviations

5.1. Correlation with terrain complexity metrics

Inspection of the deviations between wind LiDAR and met mast data in Table 7 reveals, that among the five datasets in this study, there both are examples of over- and underestimation of the wind speeds by the LiDAR measurement as compared to the met mast reference. For a vertical profiling wind LiDAR measurement near or on a hilltop or ridge, the negative (downward) curvature of the wind following the terrain contour (see schematics in Figure 1) would suggest an underestimation by the LiDAR of the true wind speed. This is in fact what is observed in the results from Sites A, B, D, and E. Site C deviates from this pattern in that at Site C the LiDAR seems to overestimate the wind conditions. Although Site C is characterized by very complex flow conditions likely caused by its situation on a slope (Table 12, Table 13), the terrain curvature at Site C (see Table 15) does not seem to be systematically different from the other sites.

This demonstrates that the flow conditions on complex terrain sites can cause both positive and negative deviations to vertical profiling wind LiDAR measurements. Potentially, this could also lead to a situation, where positive and negative influences cancel out, giving on a complex site a perfectly correct Lidar wind speed measurement by chance. Hence, prediction of the amplitude of a LiDAR/met mast error based on terrain characteristic seems to be difficult proposition.

What seems possible though, is the identification of suitable indicators among terrain complexity metrics for high errors and uncertainties for LiDAR measurements. This is also exemplified by Site C, where a peculiar result of the LiDAR/met mast comparison coincides with several of the investigated terrain characteristics (see Section 4.3) being distinct compared to the other sites.

Furthermore, the ratio of LiDAR to met mast wind speeds illustrated in Figure 7 to Figure 11 very clearly shows a systematic dependency on the wind direction. The obvious explanation for this variability is the different terrain characteristics in different wind directions, thus also suggesting a correlation of LiDAR errors with terrain characteristics.

As the deviation between wind LiDAR and met mast can have both a positive and negative sign, absolute measures have been used in the screening for possible correlations. Some examples for correlation plots thus identified are illustrated in Figure 18 and Figure 19 for the quantities "$\mathrm{range\ LiDAR/Met\ Mast}$" (see Section 4.1) and the absolute deviation from unity of the LiDAR to met mast ratio (i.e. $\mathrm{abs}(\text{"mean LiDAR/MetMast"} - 1)$). In Figure 18 and Figure 19, two additional sets of co-located, parallel LiDAR and met mast measurement from flat-terrain sites have been added to the five Sites A to E. Those two additional sites, that must not be disclosed, are situated in flat terrain and predominantly open vegetation. Even though Figure 18 and Figure 19 indeed suggest some correlations, a more rigorous statistical analysis is not sensible considering the very restricted database in this study.

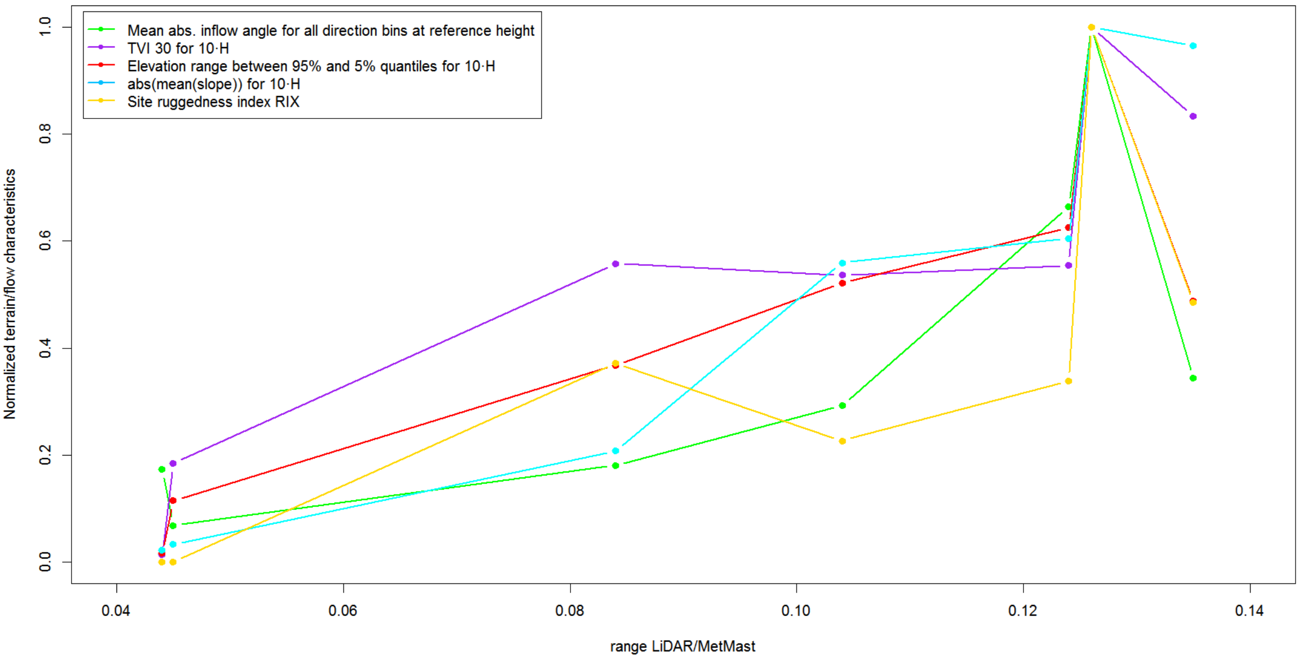

Figure 18: Correlation between the deviations between the LiDAR and the met mast measurement and characteristics for the flow and the terrain on the site. The horizontal axis gives the range of the LiDAR/met mast ratio for different wind directions (see Section 4.1). For the definition of the displayed flow and terrain characteristics, see Section 4.2 and Section 4.3.

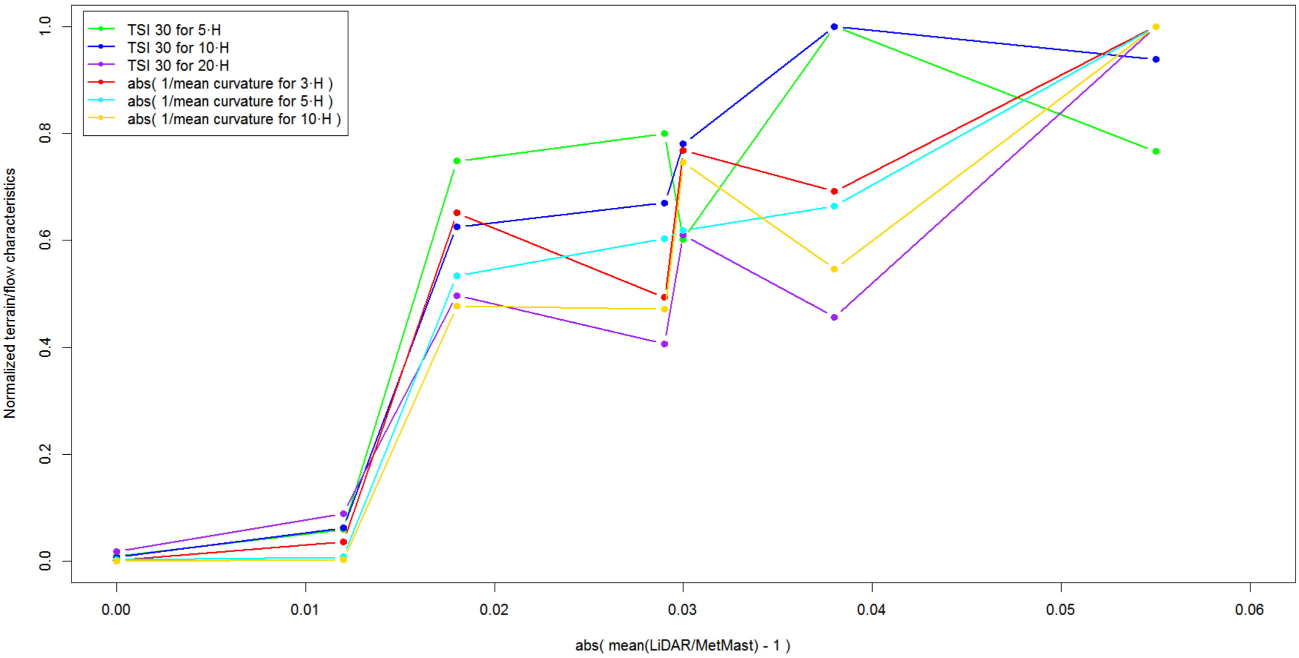

Figure 19: Correlation between the deviations between the LiDAR and the met mast measurement and characteristics for the terrain on the site. The horizontal axis gives the absolute deviation from unity for the mean LiDAR to met mast ratio. For the definition of the displayed terrain characteristics, see Section 4.3.

5.2. Correlation with wind field structure

At least for some sites (e.g. Site A), there are indications for a small intercorrelation of turbulence intensity, time of the day and LiDAR/Mast deviations.

Flow characterization shows a, in some cases very robust, dependency of TI on the time of the day. An obvious explanation for this observation is the diurnal variation of the atmospheric stratification. At the same time, analysis shows a small correlation of the LiDAR/Mast deviations with both the measured TI and the time of the day. The causality of this observation is not clear, and the effects are too small to allow a clear differentiation.

Figure 20 illustrates the correlation between the turbulence intensity and the interquartile range of the LiDAR/met mast deviation. This is not necessarily connected to terrain complexity, though, but probably only illustrates the higher measurement noise that comes with turbulence.

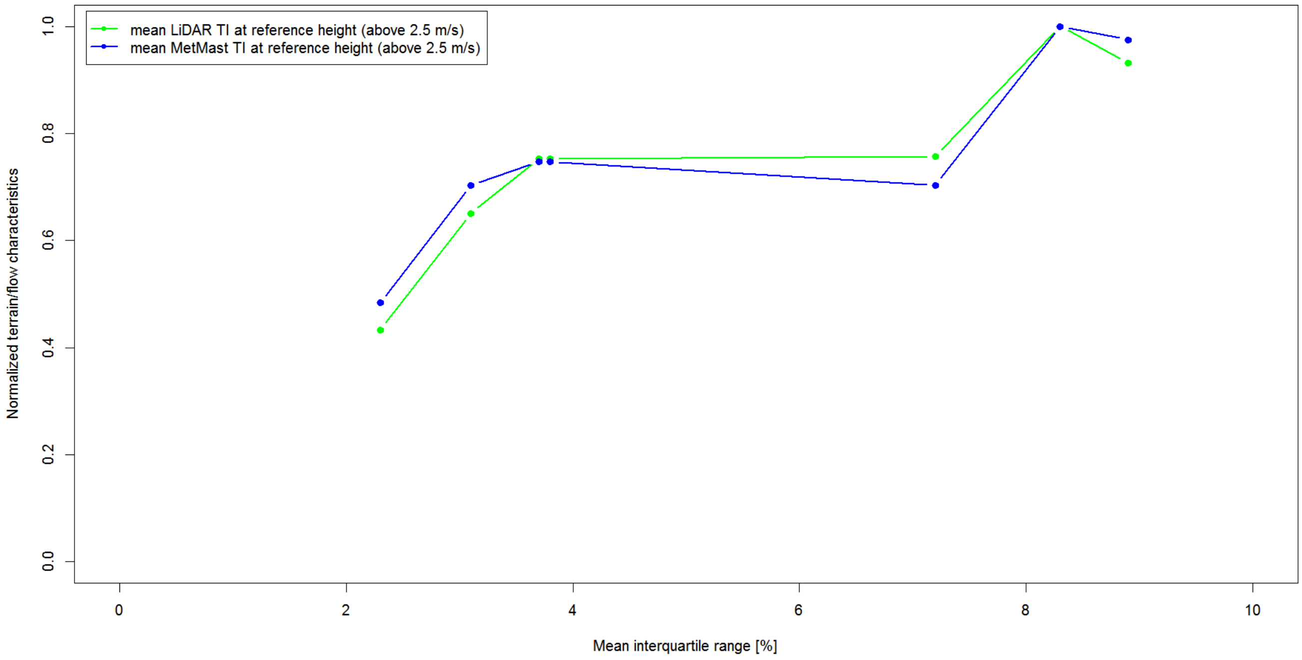

Figure 20: Correlation between the deviations between the LiDAR and the met mast measurement and characteristics for the flow on the site. The horizontal axis gives the mean interquartile range of the LiDAR/met mast ratio (i.e. the average height of the solid blue boxes in the box plots, see Section 4.1). For the definition of the displayed flow characteristics, see Section 4.2.

The data also shows a correlation between the deviations between the LiDAR and the met mast measurement and the inflow angle of the flow. The inflow angle of the flow is closely related to the terrain inclination at the site. The plot line for the inflow angle has thus been included to Figure 18.

5.3. Numerical site calibration

In order to assess the effect of the offset between measurement positions of the LiDAR and the met mast, as described in Section 1.3, a numerical site calibration has been performed for Site C. Site C shows significant deviations between LiDAR and met mast data and there are, as described in Section 5.1, indications that these deviations are in fact connected to terrain complexity. However, the distance between the LiDAR and the met mast measurement position at Site C of 42.4 m (see Table 1) could also significantly contribute to the difference in measured wind speed. Even more so, as due to the complex terrain at Site C, flow conditions are not unlikely to show a significant variation on a length scale of 42.4 m.

The assessment of the actual variation in the field would have required the erection of a second met mast (as described in Annex C of IEC 61400-12-1 (International Electrotechnical Commission, 2017)). As an approximation to this, we attempted to estimate the effect of the distance between the measurement positions from a numerical flow model computed in OpenFOAM with a horizontal resolution of 5 m.

The results for this numerical site calibration are illustrated in Figure 21. As a comparison, the bin-averaged deviations of the LiDAR/met-mast comparison have been included to Figure 21 as light blue line. The magnitude of the numerical site calibration is about of the same order than the observed differences between the LiDAR and the met mast measurement.

Application of this numerical site calibration to the LiDAR did not give a significant improvement in the LiDAR/met mast comparison and in that sense did not fare better than the complex terrain correction methods in this study.

It seems clear, however, that the offset distances between LiDAR and met mast position in complex terrain can have a significant effect and can have an amplitude comparable to the LiDAR's complex terrain error.

Figure 21: Results for the numerical site calibration for Site C for different wind directions (red line). For comparison, the bin-averaged mean deviations between the LiDAR and met mast measurement have been included as light blue line. This is the same data as shown as light blue line in Figure 9.

6. Summary & conclusions, need for further activities

Parallel vertical profiling wind LiDAR (WindCube V2) and met mast measurements from five different sites, all located in mountainous terrain in Austria, have been analyzed in this study. The comparison of the LiDAR and met mast data from these sites demonstrates that LiDAR measurements on such sites may exhibit significant measurement errors and uncertainties. Although some correlations could be identified, no obvious terrain characteristics have been identified for the prediction of complex terrain uncertainties of LiDAR measurements.

To investigate the feasibility of improving the wind LiDAR measurement in complex terrain by the calculation of corrections from numerical models, overall eleven different sets of corrections, representing different parametrizations and variants of correction methods, have been applied to the datasets. For the five considered sites, consistent satisfactorily correction of the LiDAR measurements was however not possible. The reason for this was probably the high terrain complexity of the considered sites, exceeding the domain of applicability of the correction methods. Another possible explanation is the sensitivity of scalar-averaged wind field reconstruction, such as used in the WindCube V2, to inhomogeneous turbulence, as explored by Rosenbusch et al. (2021) and Robey and Lundquist (2022).

It has become clear, that robust conclusions on the effect of complex terrain on wind LiDAR measurements and on the efficiency of correction scheme have to be based on a much broader database than the five sites in this study. An identification of robust and universally applicable limits for the deployment of wind LiDAR in complex terrain, and of correction methods to LiDAR in complex terrain, has to be based on broad and representative data, covering a representative range of geographic regions and meteorological regimes as well as a wide range of complexity from simple sites in flat and open terrain to highly complex terrain. The terrain and flow complexity measures described in Section 4.2 and Section 4.3 may be possible candidates for assessing terrain and flow complexity in such a large dataset study.

Finally, it should be noted that the observed deviations between LiDAR and met mast of up to 5% for the average wind speed do not preclude a useful application of wind LiDAR at these sites. There are several distinct use cases for the deployment of wind LiDAR in complex terrain with different requirements on the type of data and on accuracy. For some use cases (e.g. indicative wind measurements, the estimation of wind shear, measurement setups where LiDAR is combined with met masts), the observed uncertainty from terrain complexity would not preclude a successful and useful application of wind LiDAR.

7. List of References

Albers, A., Janssen, A. W., & Mander, J. (2010). How to Gain Acceptance for Lidar Measurements. *Proceedings of German Wind Energy Conference, 2010.*

Bingöl, F., Mann, J., & Foussekis, D. (2008). *Modelling conically scanning lidar error in complex terrain with WAsP Engineering Riso-R-Report, Riso-R-1664(EN).*

Black, A., Debnath, M., Lammers, A., Mazoyer, P., Schultz, R., Spalding, T., & Wylie, S. (2020, December 8). Survey of Correction Techniques for Remote Sensing Devices in Complex Flow. *IEA Task 32 Webinar*.

Clifton, A., Boquet, M., Burin Des Roziers, E., Westerhellweg, A., Hofsäß, M., Klaas, T., . . . Aitken, M. (2015). Remote Sensing of Complex Flows by Doppler Wind Lidar: Issues and Preliminary Recommendations. *Technical Report NREL/TP-5000-64634*.

Fördergesellschaft Windenergie und andere Dezentrale Energien (FGW). (2021). *Technische Richtlinien für Windenergieanlagen, Teil 6 (TR6) Bestimmung von Windpotenzial und Energieerträgen, Revision 11.*

Foussekis, D., Mouzakis, F., Papadopoulos, P., & Vionis, P. (2007). *Wind Profile Measurements using a LIDAR and a 100m Mast.*

International Electrotechnical Commission. (2017). *IEC 61400-12-1:2017 Wind power generation systems – Part 12-1: Power performance measurement of electricity producing wind turbines.*

International Electrotechnical Commission. (2019). *IEC 61400-1:2019 Wind energy generation systems - Part 1: Design requirements.*

Leelőssy, Á., Molnár, F. J., Izsák, F., Havasi, Á., Lagzi, I., & Mészáros, R. (2014). Dispersion modeling of air pollutants in the atmosphere: a review. *Cent. Eur. J. Geosci. Vol. 6, No. 3*.

Mortensen, N. G., Bowen, A. J., & Antoniou, I. (2006). Improving WAsP Predictions In (Too) Complex Terrain. *European WindEnergy Conference & Exhibition 2006.* Athens, Greece.

Robey, R., & Lundquist, J. K. (2022). Behavior and mechanisms of Doppler wind lidar error in varying stability regimes. *Atmospheric Measurement Techniques 15*, pp. 4585–4622. doi:https://doi.org/10.5194/amt-15-4585-2022

Rosenbusch, P., Mazoyer, P., Pontreau, L., Allain, P. E., & Cariou, J.-P. (2021). Wind speed reconstruction from mono-static wind lidar eliminating the effect of turbulence. *Journal of Renewable and Sustainable Energy 13*, p. 063301. doi:https://doi.org/10.1063/5.0048810

Uchida, T., & Ohya, Y. (2011). Latest Developments in Numerical Wind Synopsis Prediction Using the RIAM-COMPACT® CFD Model-Design Wind Speed Evaluation and Wind Risk (Terrain-Induced Turbulence) Diagnostics in Japan. *Energies, Vol. 4, No. 3*.

Uchida, T., & Takakuwa, S. (2020). Numerical investigation of stable stratification effects on wind resource assessment in complex terrain. *Energies, Vol. 13, No. 24*.